A spectroscopic study of the OH* radical and its application in thermometry

Chaitanya Kumar Boppana

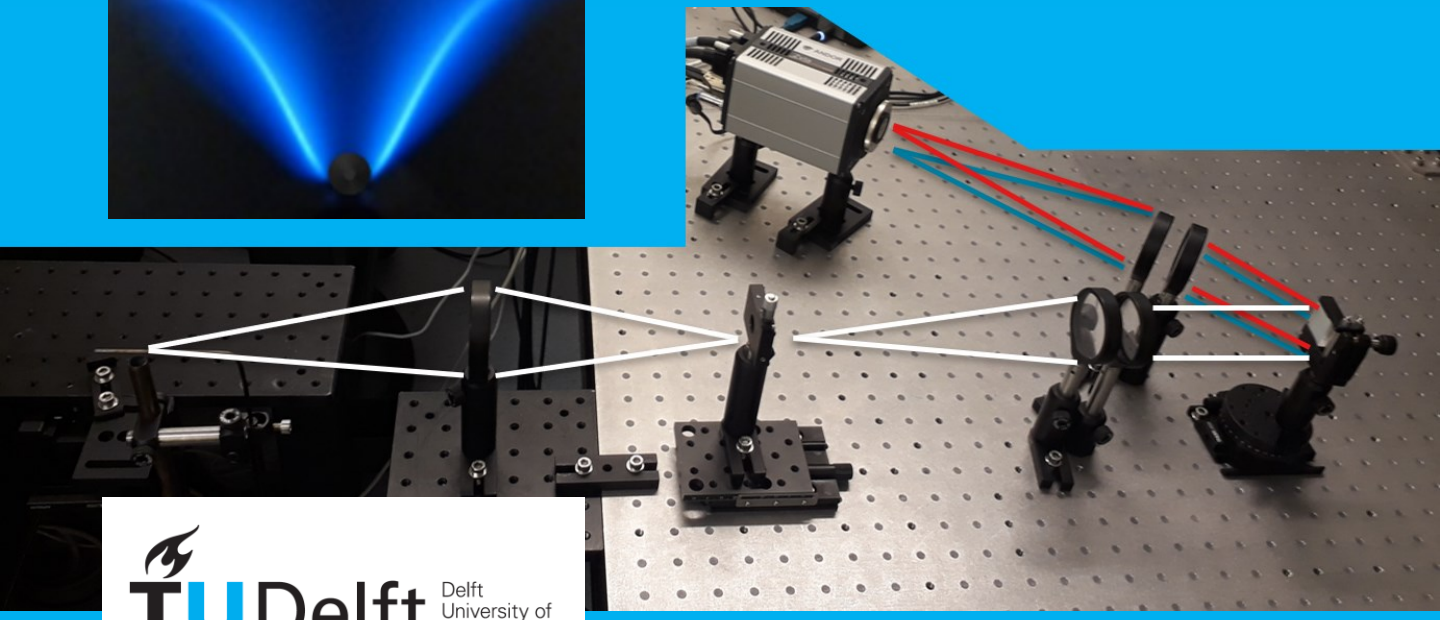

TU Delft Delft University of Technology

A spectroscopic study of the OH* radical and its application in thermometry

by

Chaitanya Kumar Boppana

to obtain the degree of Master of Science
at the Delft University of Technology,
to be defended publicly on Friday January 29, 2021 at 9:30 AM.

Student number:	4905636	
Supervisors:	Dr. ir. G. A. Bohlin	
	Dr. D. Kliukin	
	Ir. L. J. Castellanos Gonzales	
Thesis committee:	Prof. Dr. ing. G. Eitelberg	TU Delft, Chair
	Dr. ir. G. A. Bohlin	TU Delft, Supervisor
	Dr. D. Kliukin	TU Delft, Supervisor
	Dr. A. G. Anisimov,	TU Delft, Examiner
	Dr. R. Stuetzer,	DLR, Examiner

TU Delft

Preface

The journey of my master's education comes to a close with this thesis project. It has been a wonderful and inspiring ride throughout the two and half years. I would like acknowledge the contributions of the various people involved in the successful completion of my studies.

Firstly, I would like to thank my supervisor Dr. Alexis Bohlin for providing my with this opportunity to work on an exciting project. The long and interesting discussions have enabled me to broaden my thinking and instilled in me a strong scientific mentality to approach any problem. I am grateful for your patience and wisdom throughout the project.

Secondly, I am thankful to all the talented people of the Ultrafast Laser Diagnostics lab. I would specially like to thank Dr. Dmitrii Kliukin and Ir. Leonardo Castellanos for helping me with my lab work and also educating me in the field. The discussions with the team not only helped me understand my topic but also taught me about the field of diagnostics in general.

Lastly, I would never have completed this monumental journey without the love and support of my family and friends. They are foundation on which all my achievements are built. I am ever grateful for my parents for raising me in an environment where I could focus on my studies without worry. I would also like to thank all my friends here in Delft and back in India for helping me remain sane and keeping things in perspective throughout these years. I would finally like to remember my grandparents Ramachandra and Subhalakshmi who I have lost during this journey. Your presence is deeply missed.

Chaitanya Kumar Boppana
Delft, January 2021

Abstract

There is a tremendous push to explore alternative fuels such as hydrogen or synthetic fuels to combat the effects of climate change. An important step in the development of alternative fuels is the characterisation of its combustion characteristics. There are various diagnostic tools which aid in the determination of flame properties. Optical diagnostics play a crucial role by providing a non-invasive form of measurement. In the current project the idea is to utilise the passive chemiluminescence from flames to determine flame properties. The focus is on the emission from the OH^* radical present in flames. This radical is responsible for radiation in the ultraviolet region ranging from 280 nm to 350 nm. This radical was also chosen as it is a radical common to both hydrocarbon as well as hydrogen flames. The objective of the project was to develop an emission spectra model of the OH^* radical and to test its feasibility in predicting flame temperature by comparing it with emission from a laminar premixed CH_4/air Bunsen flame.

The underlying physics regarding the various aspects of the project are discussed in detail in the initial part of the part. In the latter part, the work done for the project is explained. An emission model was developed for the OH^* radical in MATLAB. The model is capable of calculating the emission spectra at different temperatures and line shapes. Then a spectrometer was built to capture the radiation from the flames in the UV region. The obtained data was post processed to get the flame spectra.

The flame spectra obtained from the flame was compared against the emission model to determine the best temperature fit. It was observed that the temperatures were much higher than the gas temperatures observed in CH_4/air flames. This is attributed to a non thermal population distribution in the excited molecules. There however exists a unique mapping to the equivalence ratio which can be utilised for equivalence ratio determination when properly calibrated. There are many possible directions uncovered to take the work further by exploring the applicability of the tool for other fuels and flame regimes.

Contents

List of Figures

List of Tables

Nomenclature

Abbreviations

ICAO	International Civil Aviation Organisation
ATM	Air Traffic Management
GHG	Greenhouse Gases
UV	Ultraviolet
IR	Infrared
MOS	Metal-Oxide Semiconductor
CCD	Charge Coupled Device
CMOS	Complementary Metal-Oxide Semiconductor
FWHM	Full Width Half Maximum
ROI	Region of Interest
ESF	Edge Spread Function
LSF	Line Spread Function
SLPM	Standard Litres Per Minute

Symbols

Greek

α	angle of incidence for grating
β	angle of dispersion for grating
λ	wavelength
μ	reduced mass for a two body system
α_e, γ_e	correction factors for the rotational constant
β_e	correction factor for the centrifugal correction factor
Λ	component of L along the inter-nuclear axis
Σ	component of S along the inter-nuclear axis
Ω	$\Lambda + \Sigma$
Ψ	wave function of the state
ν	wavenumber
η	Voigt linear combination factor

Roman

X^*	excited molecule X
E_e	energy contribution of the electron
E_v	energy contribution of the vibrational motion
E_r	energy contribution of the rotational motion
I	moment of inertia
P	angular momentum of system
r	inter-nuclear distance
r_e	equilibrium inter-nuclear distance
h	Planck's constant
c	speed of light in vacuum
J	total angular momentum of molecule
B_v	Rotational constant which is a function of the vibrational level
B_e	Equilibrium rotational constant of a non-vibrating molecule
D_v	Centrifugal correction factor which is a function of the vibrational level
D_e	Equilibrium centrifugal correction factor
F_v	rotational term value
v	vibrational level
ω	vibrational frequency in term values
$\omega x, \omega y$	anharmonicity correction factors
G_v	Vibrational term value
L	electronic orbital angular momentum
S	electronic spin angular momentum
R	rotational angular momentum of the nuclei
J_a	total electronic angular momentum
N	total angular momentum of the system without electronic spin
M	electric dipole moment
R_v	factor to account for spin splitting
a	coupling constant to account for intermediate behaviour for Hund's cases
N_n	population of state
A_{nm}	transition probability from state n to state m
$p_{J"}^{J'}$	rotational transition probability
Q	partition function
f_G	FWHM of Gaussian profile
f_L	FWHM of Lorentzian profile
f_V	FWHM of Voigt profile
T	temperature
T_{rot}	rotational temperature
T_{vib}	vibrational temperature

1 Introduction

The major driver behind most improvements in aviation technologies is the prevention of climate change. The global aviation community is working proactively to control green house gas emissions. Most companies are shifting to more sustainable fuels like synthetic fuels and hydrogen. The aircraft engine plays a major role as improvements in the engine would provide huge gains in keeping the carbon footprint in check. Eliminating combustion entirely is not feasible for long range flights as the energy density of batteries is not yet comparable to chemical energy sources such as hydrogen and fossil fuels[1]. Even though a complete elimination of emissions is preferred, the most feasible approach in terms of technology and economics is to slowly replace the current fleet with newer technologies such as alternate fuel combustors and electric-fuel hybrid aircraft.

There have been several goals outlined by various global bodies for the reduction of green house gas emissions. One such goal is set by the International Civil Aviation Organisation (ICAO) which is an agency under the United Nations. The figure 1.1 shows the projections for the emission of CO_2 from the aviation community. The figure shows the potential for improvement with the implementation of various technologies. As more improvements are made to the current generation of technologies and methods of operation, further reductions are possible to the total CO_2 emission from the aviation community. The best possible scenario is where alternative fuels are explored and implemented immediately [2].

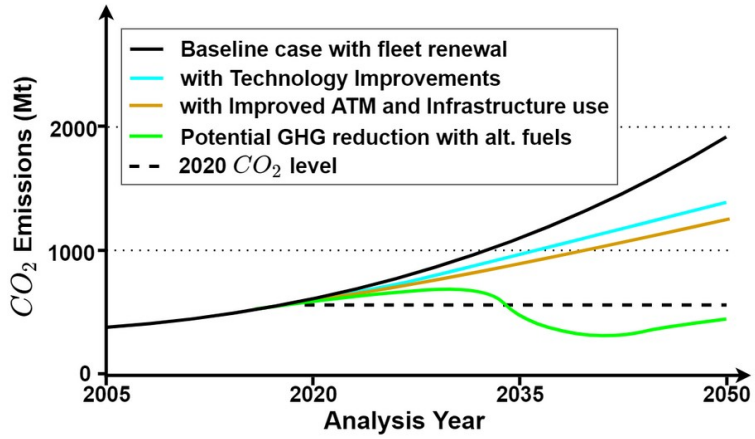

Figure 1.1: Predicted CO_2 emissions: The graph shows the reduction in CO_2 which could be achieved through technology improvements and further reduction through utilisation of alternative fuels. [2]

The ICAO has set an aspirational goal to reduce the fuel consumption by 2% per annum. Even with the most optimistic assumptions for improvements in aircraft design and operations, only a 1.37% reduction per annum can be obtained [2]. This suggests that more drastic steps need to be taken to reach the emission

goals. Alternate fuels are a good place to start and they can be implemented with least changes to current airport infrastructure.

The development of new combustor designs is a necessary part of this strategy as current combustors are optimised to handle kerosene alone. The upcoming combustors maybe designed to handle a mix of fuels or rather optimised for new fuels such as bio-fuels, methanol or hydrogen. As new technologies are being developed it also necessary to have tools to evaluate their performance. Experiments need to be conducted to evaluate the performance and be certain of the results predicted by models and theories. It is therefore necessary to have measurement tools to properly design a new concept or technology. The measurement techniques or diagnostic techniques as they are sometimes referred to as can be categorised in multiple ways. Two of the major ways of categorisation are listed below.

1. **Based on flow disturbance** - This is where the flow needs to be disturbed by external additions in the region where measurements need to be made. The technique would then be *Invasive* an example of which is the insertion of a thermocouple in a gas flow. When a physical probe is placed into a region of interest the flow maybe be disturbed leading to predictions of values which may not be true in the actual case. In such cases it is preferred to use *Non-Invasive* techniques where measurements can be taken without disturbance. An example of such techniques are optical measurement tools like Rayleigh scattering of light from a region of interest to measure properties of a fluid.

2. **Based on additional energy requirement** - In some systems to make a measurement some energy is sent into the region of interest and an output signal is obtained which contains information about the region. Such a system is known as an *Active* technique. A simple example of such a system is a flotation device to measure the water level in a flush tank. When the output signal is generated directly from the region of measurement without any additional energy sent into the system it is known as a *Passive* technique. Some examples of passive techniques are pressure gauges and thermometers.

1.1. Research Objective

The current project begins with a focus on developing tools to observe and measure the various phenomenon occurring in flames which is an important part of combustor design. Flames are further discussed in the coming chapter to gain a more clear insight into its behaviour. There are various excited radicals present in the flame which give rise to emission of photons of various wavelengths. The light emitted from flames is known as chemiluminescence which is a general term for light emission from a chemical reaction. The chemiluminescence from flames for a particular radical is being modelled in the current project. The current project focuses on the excited hydroxyl (OH^*) radical. This light emission can then be utilised to gain insight into the properties of the flame which in the current case is to determine the temperature of the flame. The technique being developed is a non-invasive and passive optical diagnostic technique for thermometry. The advantage of using such a technique is that the flow is not disturbed in its measurement and also no additional energy is needed to excite the medium to get an output signal from the flame. The light emitted from the flame is directly being studied which makes the spectrometer design a compact and easy to deploy tool at a measurement site. The exact research objective can be framed in a single sentence as follows.

To develop a spectroscopic model to predict the emission spectra of the OH radical and to test its feasibility in predicting flame temperature by comparing it with emission from a laminar premixed methane air Bunsen flame*

The current research objective can be further divided into research questions which when answered in a rigorous and systematic manner would lead to the completion of the research objective. The questions which need to be answered are listed below.

1. What is the underlying physics in diatomic molecular spectroscopy?

2. How can the emissions from the OH^* radical be modelled?

3. How does the emission spectrum from OH^* vary with temperature?

4. What experimental setup is required to capture a well resolved flame emission spectrum in the UV region?

5. How does the experimental OH^* spectrum change as a function of equivalence ratio and across the flame front?

6. Can the experimental spectrum be compared against a model to get the gas temperature?

1.2. Report Outline

This section of the report gives an outline of how the report is structured. In chapter 2 a brief introduction into flames is presented. The various radicals present in flames are discussed and their regions of light emissions are also presented. In chapter 3 a brief outline of various optical instruments are provided which would help in the design of the spectrometer. Then the physics of diatomic molecular spectroscopy is discussed in chapter 4. In chapter 5, the development of a model to predict OH^* emission spectra is discussed in detail. Then in chapter 6 the construction of the experimental setup is discussed. The various calibration steps for the setup are also discussed. Later in chapter 7 the results obtained from the experiments are discussed in detail along with a brief discussion on its comparison with literature. Finally in chapter 8 the conclusions of the project are summarised and also recommendations based on the insight gained from the project are also mentioned.

2

Combustion and Flames

In this chapter an introduction to the topic of combustion is given. The source of light emission in flames is explored deeper with an understanding of some of the major emitting radicals in flames and their wavelength regime of emission.

2.1. Basics of Combustion

Going back to the basics of chemistry, a combustion reaction can be categorised as an exothermic red-ox reaction which involves the fuel being oxidised and the oxidiser being reduced. The field of combustion is vast with innumerable contributions made over millennia. On a macro scale the reactants are consumed and the products are created with a release of heat. Upon closer inspection there exists a reaction mechanism which involves many chemical pathways and reactions which occur over a very short duration of time. This is still an area of ongoing research. The fast processes such as the ignition, quenching and chemical kinetics of intermediate species is important to study as pollutant formation is heavily dependent on these processes[3]. There are various ways of classifying combustion a few of which are discussed below.

Firstly, a distinction can be made about whether the fuel and oxidiser are mixed first and burnt or whether the fuel and oxidiser combust as they mix with one another. If the fuel and oxidiser are mixed homogeneously before combustion, then it is termed as **premixed** combustion. Premixed combustion is possible only when the fuel and oxidiser are in gaseous states. When the fuel and oxidiser are separate and combustion occurs in the region they mix, this type of combustion is known as **non-premixed** combustion. The non-premixed combustion is sometimes referred to as diffusion combustion as the molecules of the fuel and oxidiser diffuse into one another which enables the combustion to occur. In practical cases sometimes intermediate types of combustion such as **partially premixed** can often be seen where combustion starts before a perfect homogeneous mixture of the fuel and oxidiser is achieved.

Another simple way of categorising flames is based on the flow regime where the combustion occurs which could be **laminar** or **turbulent** which can be estimated using the Reynolds number whose formula is given in equation 2.1.

$$Re = \frac{\rho u L}{\mu} \tag{2.1}$$

where, ρ is the density of the fluid, u is the flow speed, L is the characteristic length scale and μ is the dynamic viscosity. When operating with pipe flows the flow is generally laminar for cases with $Re < 2000$. The combustion chemistry is dependent on the Reynolds number. An example of the influence is that in turbulent flows due to presence of eddies of all scales the mixing phenomenon is enhanced which drastically influences the time scales of combustion[3].

The ratio of the amount of fuel to the oxidiser is one of the ways of classifying a combustion process. The variation in this ratio leads to the flame having different characteristics in terms of temperature, flame stability and various other characteristics therefore it an important parameter when understanding flames. A combustion process or flame is said to be **stoichiometric** when the amount of fuel and oxidiser present completely consume each other. If the amount of fuel is higher then the mixture is termed as a fuel-rich or **rich** mixture in general. When the oxidiser is present in excess it is termed as a **lean** mixture. This can

be explained better taking an example of CH_4/air combustion. The following balanced chemical equation describes the combustion process.

$$CH_4 + 7.14\,(0.21O_2 + 0.79N_2) \rightarrow CO_2 + 2H_2O + 5.64N_2$$

Based on the equation, it can be seen that each mole of methane requires 7.14 moles of air for complete combustion and this represents a stoichiometric condition. The stoichiometric fuel to air ratio is generally represented in terms of mass which would imply that 16 g of CH_4 requires 205.92 gm of air. This gives a stoichiometric fuel to air ratio of $7.77x10^{-2}$. Another common way of discussing this mixture ratio is based on a parameter known as the equivalence ratio generally denoted by ϕ which is defined as follows.

$$\phi = \frac{\frac{m_{fuel}}{m_{oxidiser}}}{\left(\frac{m_{fuel}}{m_{oxidiser}}\right)_{stoic}} \tag{2.2}$$

Where m_{fuel} and $m_{oxidiser}$ are the masses of the fuel and oxidiser respectively. Equivalence ratio simplifies the understanding of the mixture ratio making it independent of the fuel and oxidiser being used by normalising with the stoichiometric fuel to air ratio. This simplifies the different conditions as follows.

Rich combustion	$\phi > 1$
Stoichiometric combustion	$\phi = 1$
Lean combustion	$\phi < 1$

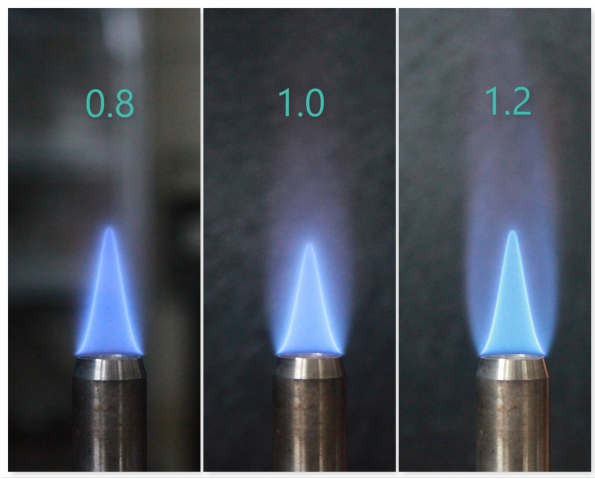

Figure 2.1: Premixed laminar methane flame in a Bunsen burner at lean, stoichiometric and rich cases with the equivalence ratio inlaid in the image. The differences in the flame are clearly illustrated. The rich flame is characterised by the prominent outer diffusion flame. The short height of the flame at stoichiometric conditions is due to a higher flame speed which is also an indicator of the equivalence ratio.

In figure 2.1 the differences in the flame for combustion cases at different equivalence ratios are shown. Even though the differences are subtle the different flames can be differentiated. A marker for rich flames is the outer diffusion flame cone which occurs due to the excess fuel being combusted with the air in the atmosphere to give an outer cone. A slight difference in colour of the flame is also seen. This is because at different equivalence ratios the emitting species are present in different relative concentrations. The height of the flame also varies with equivalence ratio which is also linked to the flame angle. The height of the flame is shortest at stoichiometric conditions because the flame speed is highest at this condition. The flame speed is linked to the flame temperature which also peaks at the stoichiometric condition[3].

2.2. Flames & Chemiluminescence

Combustion encompasses a wide variety of reactions but a flame is a canonical term used for visible regions of emission in the region of combustion. The flame is visible partly due to the emission of photons while

excited transient species undergo a transition to a lower energy state. Flames are an important component as most of the heat release happens in this region. The heat release rate can be visualised by looking at the temperature variation in a flame. For easy understanding a premixed CH_4/air combustion at stoichiometric conditions is simulated using CHEM1D which is a one dimensional laminar flame solver [4]. The results of the calculation are presented in figure 2.2.

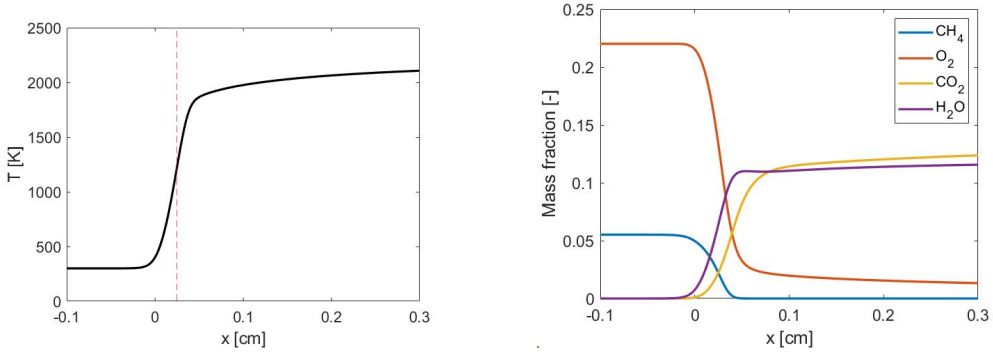

(a) Temperature profile

(b) Species mass fractions profile

Figure 2.2: The figures generated are for a premixed CH_4/air combustion at stoichiometric conditions. The variation of temperature as the reaction proceeds is clearly seen with the location of the flame front marked by a red dashed line. Also the consumption of the reactants and the production of products is shown in the species concentration profiles.

The majority of the combustion reaction occurs in a very narrow region which is the flame. The species concentration variation profile in figure 2.2 shows the narrowness of the reaction zone where most of the combustion occurs in a region less than 1 mm. A characteristic which marks the location of the flame is the flame front. There are various definitions which are generally accepted for the flame front. In the current project the location of the peak for the derivative of the temperature variation profile is chosen as the flame front. This point is also the inflection point in the temperature variation profile. In figure 2.2, the flame front is marked by the dashed red line in the temperature variation profile. It should however be noted that flameless combustion is gaining importance in the research community. This form of combustion occurs with well-distributed reaction zones. This type of combustion is being studied for controlling pollutant formation in combustion processes [5].

Chemiluminescence is an all encompassing term which refers to the light emission due to a chemical process. Combustion is a chemical process and the flame which is visible is due to chemiluminescence. The source of emission in flames could come from excited radicals and molecules and also from black body radiation. The emission ranges in the electromagnetic spectrum from UV to IR. In the current project the focus is largely on emission from excited species. The figure 2.3 shows the typical emission spectra captured from a CH_4/air flame showing the emission from the different radicals present in the flame in the wavelength limits of 275 nm to 525 nm.

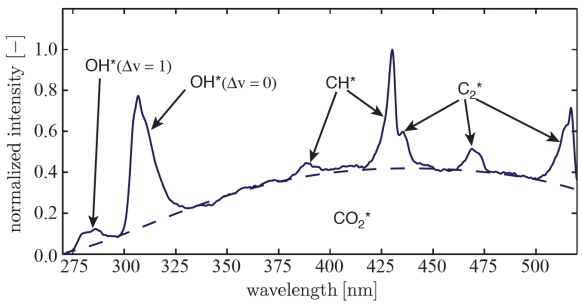

Figure 2.3: Spectra captured from a turbulent methane-air flame. The emission from OH^*, CH^*, C_2^* and CO_2^* radicals are visible. The dashed line approximates the broadband emission due to CO_2^*. [6]

In the following sub-sections a few of the emitting radicals and molecules present in hydrocarbon flames are discussed. The chemical reactions which lead to their formation are mentioned. The wavelength ranges where the emission from the radicals are observed are discussed. The particular electronic transitions which lead to these emission are also mentioned.

2.2.1. OH^*

The excited hydroxyl radical is the focus of the current project and a major source of emission in the ultraviolet region. In older standard sources like Gaydon [7] a few different equations are presented but based on recent studies the following chemical reactions are suggested in hydrogen flames[8].

$$O + H + M \rightleftharpoons OH^* + M$$

$$H + OH + OH \rightleftharpoons OH^* + H_2O$$

The two formations have been suggested by various authors but the exclusive formation pathway is still being researched. Based on a few experimental results in one study the first pathway seems to be of higher importance[8] . For hydrocarbon flames another chemical reaction is prominent.

$$CH + O_2 \rightleftharpoons OH^* + CO$$

The OH^* radical exists in the 1^{st} electronically excited state. When the molecule returns to the ground electronic state through the emission of a photon the light emitted is present in the ultraviolet region from 275 nm to 350 nm. The strongest signal is present at 306.4 nm. This transition is represented as $A^2\Sigma^+ \rightarrow X^2\Pi$. This representation is further explained in chapter 4 on spectra theory.

Another region of emission also exists for the OH^* radical in the infrared region. This emission occurs when the molecule undergoes a transition within the electronic state but across vibrational levels in that state. This emission is observed at 2.8 μm which is mixed along with emissions from H_2O^* and CO_2^* [9].

2.2.2. CH^*

The CH^* radical is the source of the blue colour seen in hydrocarbon flames. The major chemical reactions which lead to the formation of the CH^* radical are the following[10], [11].

$$C_2H + O \rightleftharpoons CH^* + CO$$

$$C_2H + O_2 \rightleftharpoons CH^* + CO_2$$

From the CH^* radical, three major systems of emissions exist which correspond to the transitions $B^2\Sigma^- \rightarrow X^2\Pi$, $A^2\Delta \rightarrow X^2\Pi$ and $C^2\Sigma^+ \rightarrow X^2\Pi$. This is also the order of intensity observed for the different transition systems. The wavelength regions in which the emission occurs are at 431.5 nm, 362.8 nm and 315 nm respectively. The transition band which occurs at 315 nm is very weak as compared to the other transition bands.

2.2.3. C_2^*

The C_2^* radical is majorly responsible for the greenish hue present in hydrocarbon flames. The chemical reaction which shows its formation is as follows.

$$CH_2 + C \rightleftharpoons C_2^* + H_2$$

There are 11 known band systems for the C_2^* radical out of which 7 band systems have been observed in flames. These 7 systems are presented in the following table with their corresponding transitions along with mentioning the strongest emission wavelengths in those systems[7], [12].

Band System	**Transition**	**Wavelengths** (nm)
Swan	$d^3\Pi_g - a^3\Pi_u$	516.52 473.71
Fox-Herzberg	$e^3\Pi_g - a^3\Pi_u$	285.5 298.7
Ballik and Ramsay	$b^3\Sigma_g^- - a^3\Pi_u$	1767.5
Mulliken	$D^1\Sigma_u^+ - X^1\Sigma_g^-$	231.27
Phillips	$A^1\Pi_u - X^1\Sigma_g^-$	1207.02
Deslandres d'Azambuja	$C^1\Pi_g - A^1\Pi_u$	410.23 385.22
Freymark	$E^1\Sigma_g^+ - A^1\Pi_u$	214.3

Table 2.1: C_2^* emission systems

Out the mentioned systems the strongest emissions correspond to the Swan system, Phillips system and the Ballik-Ramsay system. The other systems are comparatively of lower intensity and only occur in very hot flames. This is also clearly seen through the energy level diagram for the various systems which is shown in figure 2.4. The band systems which correspond to a lower energy difference are much more prominent in general flames as these excited states are easier to reach in normal flame conditions [12].

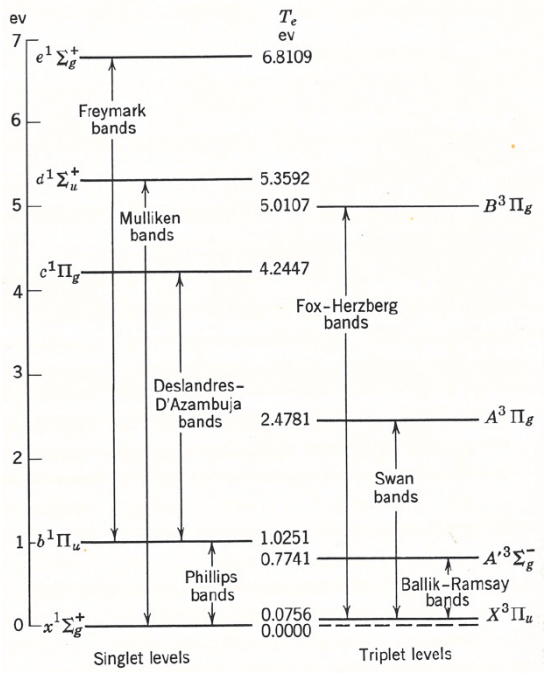

Figure 2.4: Energy level diagram for the C_2^* radical with the band systems marked. The electronic states are marked by the lowest vibrational level. [12]

2.2.4. CO_2^*

The ro-vibrational emission from the CO_2^* molecule is present as a continuum from 300 nm to 500 nm. Upon closer inspection it has been observed that a finer structure is present under the continuum. The transition which leads to the continuum emission corresponds to the $^1B_2 \rightarrow X^1\Sigma_g^+$[13]. The continuum in spectrum is due to the range of translational energies imparted to the CO_2 molecule from the colliding third body. The reaction which leads to the formation of CO_2^* molecule as follows[14].

$$CO + O + M \rightleftharpoons CO_2^* + M$$

Apart from this continuum emission the CO_2^* molecule has strong emissions in the infrared region from vibrational level transitions in the ground state of the molecule. The emissions occur at 2.8 μm, 4.4 μm and 15 μm[7], [12].

2.2.5. H_2O^*

The strongest emission in the infrared region is from H_2O^*. The strongest bands are present in the wavelength regions around 1.87 μm, 2.66 μm and 6.26 μm. Each of these emission bands would contain finer rotational structure if the resolution is made finer. The spectra for the infrared region in the wavelength range of 1.6 μm to 3.8 μm is presented in figure 2.5. The figure shows the emissions largely due to H_2O^* but also contains contributions due to CO_2^* and OH^*.

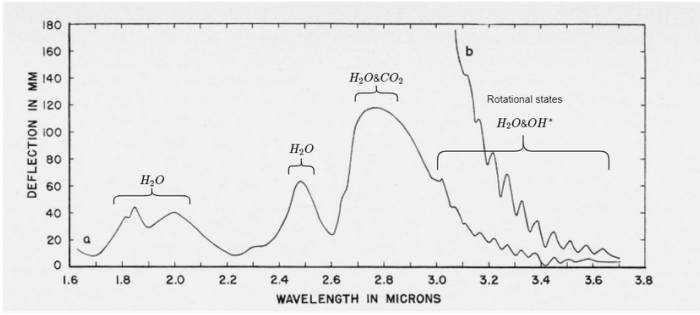

Figure 2.5: a, Infrared emission spectrum of the oxyacetylene welding torch flame with the cone of flame projected on the spectrometer slit; b, spectrum of portion of flame above the cone under similar combustion conditions [9]

3

Optics

In the current chapter some optical instruments are explained briefly. These optical instruments are necessary to build the spectrometer setup required in the project to capture the chemiluminescence from the flame. In this chapter we discuss mirrors and lenses in section 3.1 which help in relaying the light from the flame in the required direction. In section 3.2 the role gratings play in dispersing the different wavelengths of light at different angles are explained in detail. Then finally in section 3.3 the physics behind different camera sensors are discussed which capture the incoming light.

3.1. Lenses and Mirrors

When building an optical setup there is mostly always a requirement to direct light towards a capturing device with a few operations in between. The lenses and mirrors perform the role of changing the direction of light rays.

Mirrors

The basic law for the operation is the law of reflection which is defined simply as the incoming angle of the light ray should be equal to the outgoing angle with respect to the normal at the point of reflection. Figure 3.1a shows a simple case of reflection at a plane surface which clearly illustrates the principle.

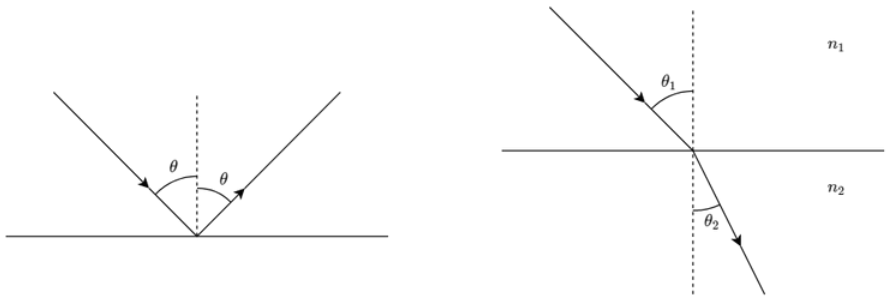

(a) Reflection (b) Refraction

Figure 3.1: A ray diagram illustrating reflection and refraction at a plane surface.

When operating with plane mirrors the calculations and angles are very clear for a beam of light but with spherical mirrors the operation is a bit more involved. Even at spherical surfaces the law of reflection is observed but at a local level. A normal perpendicular to the local surface is obtained with which the law still applies. An important parameter when working with lenses and mirrors is the focal point. The focal point is theoretically the location where beams parallel to the principal axis of the optical instrument converge. The focal length is the distance between the principal plane and the focal point. Figure 3.2 provides a clear picture for easier understanding. The equation which gives the relation between the image distance (d_i),

object distance (d_o) and the focal length (F) is given in equation 3.1.

$$\frac{1}{d_o} + \frac{1}{d_i} = \frac{1}{F} \tag{3.1}$$

The focal length is determined based on the geometry of the mirror. For simple spherical mirrors the focal length is defined as given in equation 3.2.

$$F = \frac{R}{2} \tag{3.2}$$

where R is the radius of curvature of the mirror. The radius takes positive or negative values based on whether the mirror is concave or convex respectively based on convention. The signs are not strict and can sometimes vary across texts based on which direction from the mirror or lens is considered positive.

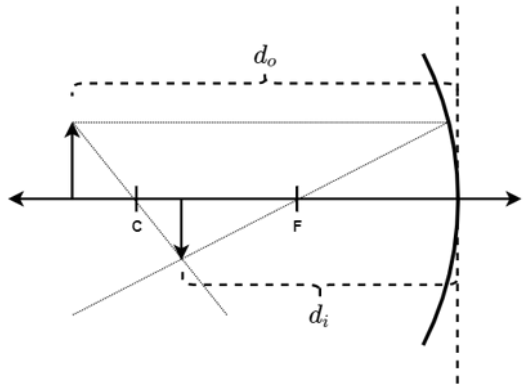

Figure 3.2: The diagram shows the image and object positions when operating with a spherical concave mirror

Lenses

The principal physical phenomenon which governs the operation of lenses is refraction. Refraction occurs when light changes direction when passing through different media with different refractive indices. The change in direction is proportional to the change in speed in the different media which is also proportional to the refractive indices of the media. Refraction can be modelled by the Snell's law which is defined as given in equation 3.3.

$$n_1 \sin\theta_1 = n_2 \sin\theta_2 \tag{3.3}$$

The angles θ_1 & θ_2 are measured with respect to the normal at the point where refraction occurs. The refractive indices of the two media are n_1 & n_2. Refraction at a plane surface is illustrated in figure 3.1b which shows the different media and the angles involved.

Lenses are made using the principle of refraction to divert the path of the light rays which can then be useful in projecting objects or performing further operations with the light. The application of Snell's law on curved surfaces is similar to the reflection case where a local normal provides the angles for the calculation of the light path. Overall the equation which provides a relation between the object distance and the image distance is the same as in the case of mirrors which is given by equation 3.1. The difference occurs in the calculation of the focal length. The focal length for a regular spherical lens is calculated as given in equation 3.4 [15].

$$\frac{1}{F} = (n-1)\left[\frac{1}{r_1} - \frac{1}{r_2} + \frac{(n-1)\,t}{n r_1 r_2}\right] \tag{3.4}$$

Where n is the refractive index of the lens material, refractive index of air is assumed as 1, r_1 & r_2 are the radii of curvature of the lens and t is the thickness of the lens. The image distance and object distance are also not measured from the centre of the lens but from principal planes whose location is defined by the following equations 3.5. The figure 3.3 shows the principal planes and also clearly illustrates the distances from equations 3.1 and 3.5.

$$\begin{aligned} d_1 &= F t\left(\frac{1-n}{r_2}\right) \\ d_2 &= F t\left(\frac{1-n}{r_1}\right) \end{aligned} \tag{3.5}$$

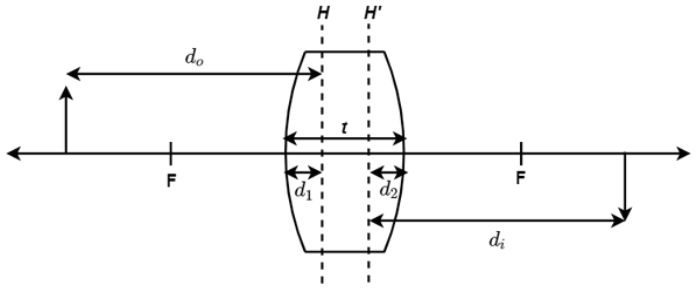

Figure 3.3: The diagram shows the location of principal planes (H and H') in a thick spherical lens (Eq.3.5) from which the measurements of the object and image distances are taken which are d_o and d_i respectively.

In most optical setups the image and object distances are much larger than the thickness of the lens which leads to a simplification of the expression for focal length to equation 3.6.

$$\frac{1}{F} = (n-1)\left[\frac{1}{r_1} - \frac{1}{r_2}\right] \tag{3.6}$$

When the object and image distances are calculated for different scenarios the table 3.1 is generated in the case of a concave lens. This table is useful to keep in mind when designing an optical setup.

Object distance	**Image distance**	**Magnification**
$d_o < F$	Virtual Image	-
$d_o = F$	$d_i = \infty$	$M = -\infty$
$F < d_o < 2F$	$\infty > d_i > 2F$	$-\infty < M < -1$
$d_o = 2F$	$d_i = 2F$	$M = -1$
$2F < d_o < \infty$	$2F > d_i > F$	$-1 < M < 0$

Table 3.1: Image and object distances for different scenarios with a concave lens along with magnification in the image observed

The magnification of the image can be estimated in both lenses and mirrors with the help of equation 3.7 using the image and object distances. If the magnification is negative it implies that the orientation of the image is reverse to that of the object. The negative is again as mentioned earlier subject to the notation used in the calculations.

$$M = -\frac{d_i}{d_o} \tag{3.7}$$

3.2. Gratings

Gratings or diffraction gratings are optical tools which help in dispersing incoming light at various angles based on the wavelength of the light. Gratings operate based on the principle of interference of light waves which requires a basic understanding of wave physics. When two waves with the same frequency meet they interfere with one another to produce a single wave with different amplitude and/or phase to the first two waves. The phase difference between the two waves determines whether the waves interfere constructively or destructively. This is also illustrated through the figure 3.4 which shows when the waves are in phase and out of phase by 90^o which correspond to constructive and destructive interference respectively.

(a) Constructive interference

(b) Destructive Interference

Figure 3.4: Interference of two waves of amplitude A and B are shown. In constructive interference as they are in phase the final wave has an amplitude of A+B. In the case of destructive interference the waves are out of phase by 90^o giving an amplitude of A-B for the final wave.

A grating is manufactured in such a way that different wavelengths are dispersed at different angles based on interference. The surface of the grating is composed of periodic elements such as ridges or grooves from which the light is refracted or reflected based on whether the grating is a transmission or reflective type respectively. Each of these ridges acts as a new source of light based on the Huygens-Fresnel principle. At certain angles certain wavelengths of light undergo destructive or constructive interference allowing the light to exit only at certain angles. There are various kinds of gratings available in the market. They can be transmission or reflective gratings based on their materials. They can also be differentiated based on manufacturing such as ruled or holographic where ruled gratings are mechanically cut by precise machines whereas holographic gratings are manufactured using intense monochromatic light to etch photosensitive materials [16].

The operation of the grating is governed by the grating equation which is provided in equation 3.8.

$$m\lambda = d\left(\sin\alpha + \sin\beta\right) \tag{3.8}$$

where m is the order of the dispersion, λ is the wavelength of light, d is the spacing between the ridges, α is the angle of incoming light with respect to the normal of the grating plane and β is the outgoing angle with respect to the normal. In the current section the angles measured counter-clockwise from the normal are considered positive. Figure 3.5 provides an illustration of the angles involved in the dispersion process at the grating surface.

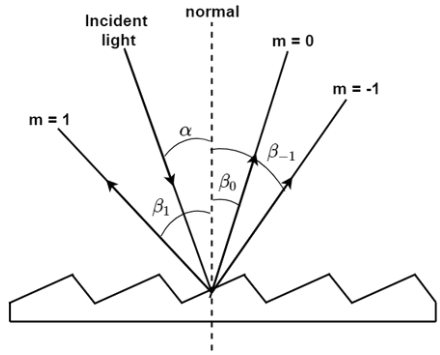

Figure 3.5: The diagram illustrates the angles involved in the dispersion with a grating. The diagram shows the dispersed light with orders m = -1, 0 & 1.

At the condition where the order of dispersion is zero (m=0), no dispersion is observed and all the light passes through or is reflected. In the case of a reflective grating, it is known as *specular reflection*. The efficiency of the grating is the amount of light dispersed with respect to the incident light in the given spectral order. The efficiency of the grating is dependent on the wavelength and angle of incidence of the incoming light. For a fixed wavelength of light the efficiency is maximum at the *Littrow condition*, which is when the angle of both the incoming light and the diffracted light is the same. In the case of a reflective grating, the dispersed light would then be in the same direction as the incoming light.

Gratings are mainly used to separate light of different wavelengths spatially. Hence an important parameter which needs to be defined when operating with gratings is the *angular dispersion*. Angular dispersion is the amount of separation between between light rays of different wavelengths. Angular separation can be obtained by differentiating equation 3.8 to obtain the change in the dispersed angle per unit change in wavelength which is expressed in equation 3.9.

$$D = \frac{d\beta}{d\lambda} = \frac{m}{d\cos\beta} = \frac{\sin\alpha + \sin\beta}{\lambda\cos\beta} \tag{3.9}$$

Based on equation 3.9 it can be observed that for a given dispersion angle, the angular dispersion can be increased by observing higher order dispersion or using gratings with smaller groove spacing. These parameters cannot be chosen independently but are related to the angles involved. By substituting the grating equation in the term for angular dispersion, the equation can be converted to consist only the operating angles and the wavelength of light to obtain a more general expression.

Another important phenomenon involved in the operation of gratings is *anamorphic magnification*. This phenomenon is the skewing of the width of light beams in the plane of dispersion. This phenomenon is entirely dependent on the angles involved in the dispersion process and is clearly illustrated in figure 3.6. The anamorphic magnification is calculated as given in equation 3.10.

$$A = \frac{b}{a} = \frac{\cos\beta}{\cos\alpha} \tag{3.10}$$

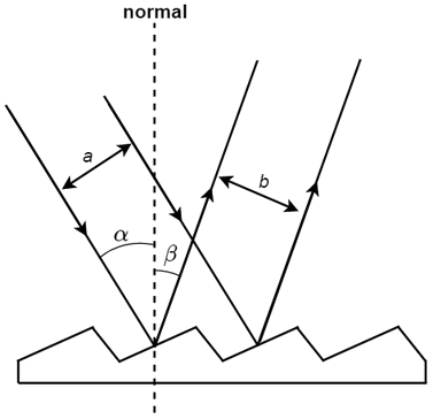

Figure 3.6: The diagram illustrates the changing of beam width due to the change in angles in the dispersion process which leads to an anamorphic magnification. The shown beam width changes from '*a*' to '*b*'.

3.3. Image Sensors

Image sensors are necessary to capture light signals for further analysis. In our application we need the image sensors to capture the light emitted from the flame. Previously image sensors were manufactured using chemicals which react when illuminated under light. This was using photographic films and plates which are exposed to light which etch an image on the film based on the light exposure in each location. Nowadays most of the imaging needs are satisfied through digital imaging rather than chemical imaging. Digital imaging has developed based on the Metal Oxide Semiconductor (MOS) technology which operates by controlling the electrical conductivity of a semiconductor by applying a voltage.

The principal operating phenomenon in light detection through digital sensors is the photoelectric effect. The photons dislodge electrons in the semiconductor material which is then analysed further. The differences in how generated charge is handled leads to different sensor types. Current digital image sensors are mostly of two types CCD (Charge Coupled Device) and CMOS (Complementary-MOS) which are discussed in detail in following sections.

CCD Sensors

The charge coupled device (CCD) was developed in 1969 at Bell Labs by Willard Boyle and George B.Smith for which they have also received the Physics Nobel Prize in 2009. The CCD sensors are made up of MOS capacitors which are connected in arrays. Each pixel consists of a depleted capacitor which accumulates charge proportional to the amount of light at that location. An external controller can move the charge from one capacitor to the next by varying the controlling voltage on the metal gate. At the end of the array the charge in the potential well is readout through an amplifier to obtain a complete matrix of the charge contained in each pixel. This data is processed to obtain a picture [17].

The major consideration when operating with CCD sensors is handling light during readout which is known as shuttering. There exists a finite time when readout occurs during which the light still falls on the pixels which can affect the quality of the image by introducing smearing. If the readout speed is increased it leads to an increased noise level in the image. This problem can be solved by physically blocking the light by introducing a mechanical shutter but this introduces problems as a mechanical shutter has lifetime issues, is power intensive and are relatively slow.

There are different architectures implemented to optimise the operation of the CCD sensor for different applications. The basic architecture without any additions is known as a full frame sensor where the entire

arrays need to be read before the next exposure. This architecture is most sensitive to light but is also most prone to smearing. The frame transfer architecture is another architecture which uses a two part sensor. One part is sensitive to light whereas the other part is covered with an opaque mask. After an exposure the charge is rapidly shifted from the light sensitive part to the opaque part which is then read. Even though there exists smearing when the charge is transferred from the light sensitive part to opaque part, it is much less than a full frame CCD. This architecture also allows for a higher frame rates but the disadvantage is the cost due to the requirement of a larger sensor. The other architecture which drastically reduces smearing is the interline transfer CCD which involves using transfer channels to move charge which are covered by an opaque mask. This process practically removes smearing but the disadvantage is that the sensitivity to light reduces as a portion of the sensor is made opaque [18]. The figure 3.7 shows the schematics of the mentioned CCD architectures for a better understanding.

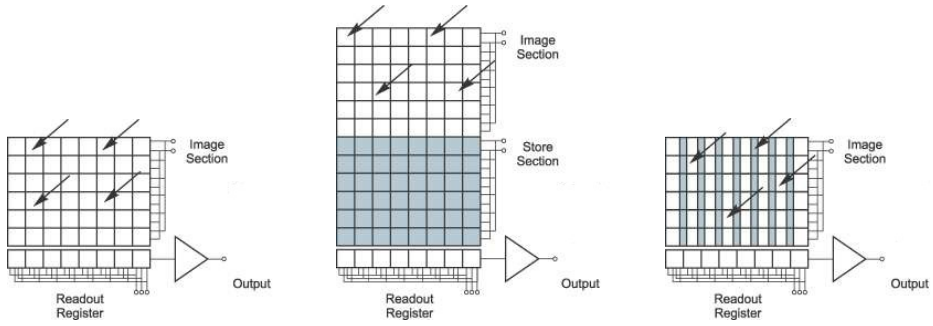

(a) Full Frame CCD (b) Frame Transfer CCD (c) Interline CCD

Figure 3.7: The images show the schematics of a few CCD sensor architectures.[18]

CMOS Sensors

Complementary-MOS is actually a fabrication process for MOS transistors. The commonly known CMOS sensor refers to an active pixel sensor utilising the CMOS fabrication process. Active pixel sensor implies that the pixel not only acts a photo detector but also consists of one or more transistors which allow for an intra-pixel readout. The first practical CMOS sensor was presented in 1993 by Eric Fossum working at Jet Propulsion Laboratory (JPL),USA [19]. The idea was that including intra-pixel readout would eliminate charge transfer thus eliminating smearing and allow for faster frame rates.

The most common shuttering technique is the rolling shutter. This is a technique where all the pixels do not read out at the same instant but they readout in a series of arrays across the pixel matrix. This introduces artefacts when capturing highly dynamic objects. The compromise with rolling shutter allows for higher frame rates. The major advantage of using CMOS sensors is the cost. The utility of the CMOS fabrication technique in a wide range of applications enables manufacturers to take advantage of bulk production to reduce overall costs. CMOS sensors are also rapidly improving with each generation of the technology.

Comparison

When working with an imaging device it is important to determine the best sensor for that particular application. Each of the sensor has their advantages and disadvantages [20], [21].

As mentioned earlier the cost of a CMOS sensor is lower than a CCD sensor due to bulk production for a range of commercial products which reduces the overall cost of production. Just a few decades earlier most commercial imaging devices utilised CCD sensors but CMOS sensors have developed rapidly and will continue to improve in the coming future.

The CCD sensor operates on the principle of charge transfer across capacitors which has a disadvantage of blooming. This phenomenon can be easily understood as charge getting out of the potential well at a location and overflowing into the neighbouring wells when overexposed. This produces streaks in the direction of the charge transfer arrays in the image when imaging bright spots. This problem does not exist in CMOS sensors.

The CMOS sensor has issues with rolling shutter when imaging a highly dynamic scene. A global shutter can be implemented to mitigate this problem but would reduce the frame rate of operation. Similarly the problem of smearing exists in CCD sensors due to its shuttering which is overcome with different architectures which come at the cost of light sensitivity. Overall the CMOS sensor is much more suited for faster read

speeds also with lower read noise.

In terms of the light sensitivity, the CCD sensor is still a more preferred option. In a CMOS sensor a portion of the pixel is lost to circuitry which reduces its light sensitivity. Also due to reflections from the metal circuitry, the overall noise level of the image is higher. These reasons contribute to the use of CCD sensors for applications where light sensitivity is a major focus such as astronomy.

It should be noted that there does not exist a clear better option when comparing CCD and CMOS sensors. The choice of sensor is based on the requirements of the application. General cameras have a low efficiency when capturing light in the UV region so a highly light sensitive camera would be required for the current project. CCD sensors provide a better light sensitivity and are hence the ideal choice for the project. Also no high speed imaging is required for the current project as a stationary flame is observed. This removes the necessity for a CMOS sensor. The cost however is lower for a CMOS sensor which is an important factor. Finally the sensor used in project was a CMOS sensor based on the availability in the lab. The low light sensitivity was compensated by using high exposure times.

4

Diatomic Spectra Theory

Spectroscopy is the measurement of radiation intensity as a function of wavelength. This field involves the interaction of matter with photons. When light strikes a molecule, the energy of the photon is transferred into the molecule pushing it to a higher energy state. This results in an absorption spectra. This process can occur in the reverse direction as well giving an emission spectra. To understand the spectra obtained from a any molecule or radical, its molecular structure needs to be understood. The energy levels present in the molecule combined with the information for allowed transitions provide a picture of the spectra that can be expected from a molecule. In the current chapter the theory presented is largely focused on diatomic molecules as the purpose of the project involves the study of the OH^* radical.

4.1. Energy Levels

Before a spectra is obtained the various energy levels of the molecule need to be characterised. The energy of the molecule which is involved in spectroscopy can be split into three parts - electronic (E_e), vibrational (E_v) and rotational energy (E_r).

$$E = E_e + E_v + E_r \tag{4.1}$$

The descending order of energies is $E_e > E_v > E_r$. Based on this understanding it appears like for each electronic state there exist many vibrational states within which many rotational states exist. Each of these energies will be discussed in detail based on which spectra is obtained by transitions among these levels.

4.1.1. Rotational Energy

The most simple model to represent the rotational energy of a diatomic molecule is the rigid rotor model. This model is represented by two point masses connected by a rigid massless rod. The figure 4.1 .The rotational energy of the system is given as follows.

$$E_r = \frac{1}{2} I w^2 = \frac{P^2}{2I} \tag{4.2}$$

where I is the moment of inertia of the system, w is the angular velocity and P is the angular momentum of the system. The moment of inertia in a rigid rotor model can be calculated as given in equation 4.3.

$$I = \mu r^2 \tag{4.3}$$

where $\mu = \frac{m_1 m_2}{m_1 + m_2}$ is the reduced mass of the system and r is the inter-nuclear distance.

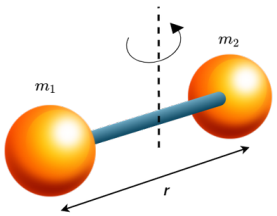

Figure 4.1: The diagram shows the simple rigid rotor model which consists of 2 point masses connected by a rigid massless rod.

The molecules need to obey wave mechanics which only allow certain discrete energy states. By applying the principles of wave mechanics and solving the Schrödinger equation for the rigid rotor model the energy equation 4.2 converts to equation 4.4 [22].

$$E_r = \frac{h^2}{8\pi^2 I} J(J+1) \tag{4.4}$$

where h is the Planck's constant and J is the rotational quantum number which varies from 0,1,2,...

In molecular spectroscopy the energy is generally written in the form of *term values* which is the energy value divided by hc where c is the speed of electromagnetic radiation in vacuum. This term values are generally represented in the units cm^{-1} which is the wavenumber.

$$F(J) = \frac{E_r}{hc} = BJ(J+1) \tag{4.5}$$

where B is the rotational constant.

$$B = \frac{h}{8\pi^2 cI}$$

In practical applications, the diatomic molecule does not behave perfectly as a rigid rotor. The inter-nuclear distance would vary with the centrifugal force experienced by the molecule. This implies that the rotational term value would have correction terms to the initial equation to perfectly model the molecule giving equation 4.6.

$$F(J) = BJ(J+1) - DJ^2(J+1)^2 + ... \tag{4.6}$$

where D is the correction factor.

Another important aspect to take into account is that the rotation and vibration of the molecule occurs simultaneously. This implies that the inter-nuclear distance is constantly changing which also affects the moment of inertia of the molecule. Based on this phenomenon the rotational constant B and the correction factor D are also dependent on the vibrational level v of the molecule.

$$\begin{aligned} B_v &= B_e - \alpha_e\left(v + \frac{1}{2}\right) + ... \\ D_v &= D_e + \beta_e\left(v + \frac{1}{2}\right) + ... \end{aligned} \tag{4.7}$$

where B_v & D_v are the vibrational level dependent terms and B_e & D_e are the constants calculated as per the equilibrium inter-nuclear distance. The constants α_e and β_e are dependent on the vibrational motion of the molecule. Due to these changes the final rotational term value expression is given as per equation 4.8.

$$F_v(J) = B_v J(J+1) - D_v J^2(J+1)^2 + ... \tag{4.8}$$

4.1.2. Vibrational Energy

Similar to the approach followed in the case of rotational energy, the vibrational energy is estimated from a simple model known as the harmonic oscillator. A harmonic oscillator consists of two point masses connected by a simple spring which is illustrated in figure 4.2. The potential energy of the system can be expressed as follows.

$$E_v = \frac{1}{2}kx^2 = \frac{1}{2}k(r - r_e)^2 \tag{4.9}$$

where r_e is the equilibrium inter-nuclear distance and k is the spring constant which is based on the attractive forces between the two nuclei of the molecule.

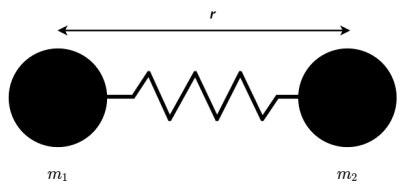

Figure 4.2: The diagram shows a harmonic oscillator which consists of 2 point masses connected by a simple spring.

The force constant can be expressed in terms of the oscillation frequency (ν_{osc}) and reduced mass (μ) of the system.

$$k = 4\pi^2 \mu \nu_{osc}^2 \tag{4.10}$$

When the simple harmonic oscillator is extended to include wave mechanics the energy of the system is expressed as per equation 4.11 [22].

$$E_\upsilon = h\nu_{osc}\left(\upsilon + \frac{1}{2}\right) \tag{4.11}$$

where υ is the vibrational quantum number which takes the values 0,1,2,...

The vibrational energy is also expressed in term values as follows.

$$G(\upsilon) = \frac{E_\upsilon}{hc} = \omega\left(\upsilon + \frac{1}{2}\right) \tag{4.12}$$

where $\omega = \frac{\nu_{osc}}{c}$ is the vibrational frequency in term values.

The molecules do not behave as per the harmonic oscillator model but as an anharmonic oscillator. The Morse potential function is often used to approximate the anharmonic oscillator. The potential curve of an anharmonic oscillator is shown in figure 4.3. When the Morse potential is incorporated into the vibrational energy expression, the term value expression changes into equation 4.13.

$$G(\upsilon) = \omega_e\left(\upsilon + \frac{1}{2}\right) - \omega_e x_e\left(\upsilon + \frac{1}{2}\right)^2 + \omega_e y_e\left(\upsilon + \frac{1}{2}\right)^3 + ... \tag{4.13}$$

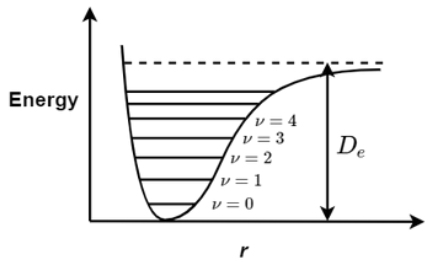

Figure 4.3: The figure shows a Morse potential curve along with a few vibrational levels. The figure also shows the disassociation energy (D_e) for the potential curve at that particular electronic state.

The energy equation 4.13 is represented with the minimum based on the potential minimum as the zero energy position. When the lowest energy is located at the position of the zeroth vibrational level, the vibrational term expression changes into equation 4.14.

$$G_0(\upsilon) = \omega_0\upsilon - \omega_0 x_0 \upsilon^2 + \omega_0 y_0 \upsilon^3 + ... \tag{4.14}$$

4.1.3. Electronic States & Energy

The electronic energy of the molecule is represented with the term symbol T_e when used along with the vibrational and rotational term expressions. The most important parameters which describe the electronic state is presented by two quantum numbers which are Λ and S. The quantum number Λ is the component of the resultant orbital angular momentum (L) along the inter-nuclear axis. The quantum number Λ can only take integer values. The electronic energy depends on the absolute value of Λ which are represented by capital Greek alphabets. Thus $|\Lambda|$ = 0,1,2,3,... are represented by Σ, Π, Δ, Φ,... respectively.

The resultant spin angular momentum of the electrons in the molecule is given by S. The quantum number S can take half integer and integer values. The resultant spin S can be projected onto the inter-nuclear axis giving the vector Σ. Note that Σ should not be confused with the state Σ for $\Lambda = 0$. The vector Σ can take the values -S,-S+1,..., S-1,S. This gives rise to 2S+1 degenerate states with slightly different energy. This is due to the interaction between the electronic spin and electronic orbital angular momentum. This is known as spin splitting. This degeneracy is given the number $M = 2S + 1$ which is the multiplicity [7].

The term symbol notation used in representing the different electronic states will be expanded upon for a clearer understanding. The multiplicity is given as a superscript before the quantum number Λ. For example

the expression $^3\Pi$ implies that the spin multiplicity $M = 3$ with $S = 1$ and the quantum number $\Lambda = 1$. As various electronic states can have the same characteristics the expression is preceded by letters of the English alphabet to distinguish between the different states. The ground state is represented as X with the higher excited states represented as A, B, C,... in the order of increasing energy of the electronic states. If different multiplicities exist for the same molecule then smaller case letters a,b,c,.. are used for the states with the different multiplicity.

Before proceeding into the next sections all the different angular momenta present in the system are presented in a list for a clear understanding.

- **L** - electronic orbital angular momentum
- **S** - electronic spin angular momentum
- **R** - rotational angular momentum of the nuclei
- $\mathbf{J_a = L+S}$ - total electronic angular momentum
- $\mathbf{J = J_a+R}$ - total angular momentum of the system
- **N = J-S** - total angular momentum of the system without electronic spin

Coupling cases

In the previous section the electronic states are discussed without the influence of vibrational and rotational motion of the molecule. Due to interaction of the rotational motion, electronic orbital momentum, electronic spin and the rotation of the nuclei various interesting coupling phenomenon are observed. This coupling phenomenon changes the equation of the rotational term expression to include the electronic orbital angular momentum Λ in the general case [12], [22], [23].

$$F_v = B_v \left[J(J+1) - \Lambda^2 \right] \tag{4.15}$$

The interaction between the rotation of the nuclei and the electronic orbital angular momentum has an influence on the energy levels of the $-\Lambda$ and $+\Lambda$ states. Initially it was mentioned that both of them have the same energy but when the coupling is taken into account they produce doubly degenerate states. This degeneracy is known as Λ-doubling. For the degeneracy to occur the positive and negative components of Λ should be present, therefore the Λ-doubling occurs for all Λ's except $\Lambda = 0$ which is the Σ state. The difference in energy is proportional to $J(J+1)$ therefore the rotational levels is split into two close levels. The difference in energy is very small compared to the overall difference between the rotational levels of different J values. The effect becomes more pronounced in higher J states.

The coupling between the different angular momenta of the system was presented by F. Hund in 1927 who defines 5 coupling cases. In the current project only the first two cases are discussed which are the most important for diatomic molecules.

Hund's case (a) - In this case the rotational angular momentum of the nuclei is very weakly coupled with the electronic orbital angular momentum. The electronic spin and orbital angular momentum are strongly coupled. The electronic motion is also strongly coupled to the inter-nuclear axis. In this case the the electronic orbital angular momentum is replaced by the total electronic angular momentum ($\Omega = \Lambda + \Sigma$) in the rotational term expression presented in equation 4.15.

$$F_v(J) = B_v \left[J(J+1) - \Omega^2 \right] \tag{4.16}$$

Hund's case (b) - For this case the electronic spin of the system is very weakly coupled with the inter-nuclear axis. The rotational angular momentum of the nuclei is however strongly coupled with the electronic motion. In this particular case the rotational term would remove the spin term S from the total angular momentum of the system leading to the following equation.

$$F_v(J) = B_v \left[N(N+1) - \Lambda^2 \right] \tag{4.17}$$

In reality most diatomic molecules do not follow any case perfectly but are an intermediate between the two cases which is incorporated using a coupling constant in the rotational term expression.

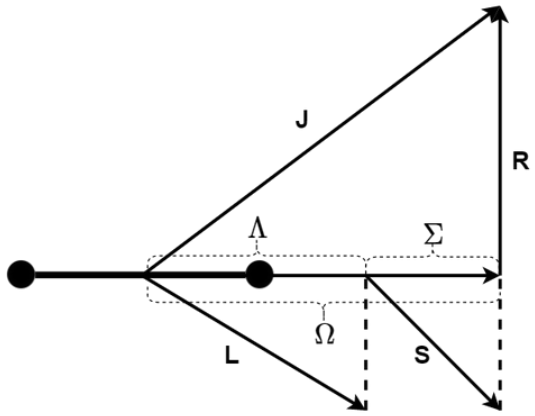

Figure 4.4: The diagram shows the different angular momentum vectors and their projections on the inter-nuclear axis. The presented system is for the Hund's case (a) where the L and S vectors are strongly coupled with the inter-nuclear axis. The total angular momentum J of the system is obtained by adding the projected vector Ω and R.

4.2. Transitions

In the previous sections all the different possible energy states of the molecule have been discussed. It should however be noted that all possible transitions are not observed in a spectra. Only certain transitions are allowed in a molecule which will be elaborated upon. Even in the allowed transitions, all transitions are not equally likely. Transitions between certain states are more likely than others.

The common notation in representing transitions in molecular spectroscopy is $A-B$ in general with A being the upper state and B being the lower state. $A \rightarrow B$ and $A \leftarrow B$ can also be used to indicate emission and absorption respectively [22].

4.2.1. Selection Rules

To determine which transitions are possible a transition moment needs to be calculated with the wave functions of the upper and lower states.

$$R = \int \psi' M \psi'' d\tau \tag{4.18}$$

where R is the transition moment, M is the electric dipole moment, ψ' and ψ'' are the wave functions of the upper and lower states respectively. If the transition moment is zero the transition is forbidden and for non-zero values of the transition moment the transition is allowed. The wave functions are related to the quantum numbers of the upper and lower states based on which a few selection rules can be extracted.

The selection rule which applies to all molecules in general is based on the total angular momentum quantum number J. The rule is

$$\Delta J = 0, \pm 1$$

This rule however has an exception which is $J = 0 \not\rightarrow J = 0$. This is a general principle which applies to all cases but a few selection rules are applicable based on the Hund's coupling case of the state involved. For Hund's case (a) the spin is strongly coupled with the orbital angular momentum which defined the quantum number Ω which follows the following rule.

$$\Delta\Omega = 0, \pm 1$$

In the case of Hund's case (b) the quantum number N is defined which follows the selection rule.

$$\Delta N = 0, \pm 1$$

Apart from these particular rules there are a few selection rules which are applicable to both the Hund's cases (a) and (b).

$$\Delta\Lambda = 0, \pm 1$$
$$\Delta S = 0$$

This implies that the molecules are allowed to transition between states with the same multiplicity and among electronic states following the rule for Λ. It should be noted that molecules exist as an intermediate between the coupling cases therefore the particular selection rule for a particular Hund's case may not be a strict selection rule but the transitions which follow the rule would be more likely to occur. When transitions occur between states from Hund's case (a) to case (b) or vice versa, the rules which are common to both the cases are strictly followed [12], [23].

4.2.2. Line Intensities

The line positions can be determined based on the energy levels and the allowed transitions. However as mentioned earlier not all transitions are equally likely. When transitions occur across rotational, vibrational and electronic states, the transitions moment determines the probability of the transition but the intensity of the emission is also dependent on the population of the initial state and the wavelength of the transition itself.

An important concept when discussing spectra with an electronic transition system consisting of different vibrational band systems is the *Franck-Condon Principle*. The selection rules do not apply any restriction on transitions among any vibrational levels. Still there exist vibrational level transitions which are more likely than others. The main concept of the idea is that *"the electron jump in a molecule takes place so rapidly in comparison to the vibrational motion that immediately afterwards the nuclei still have very nearly the same relative position and velocity as before the jump"*. In the wave-mechanical understanding the transition among vibrational levels with the most overlap in the same inter-nuclear distance are most likely. These transitions then would have the highest relative intensity in the system. The figure 4.5 shows an illustration for a clearer understanding.

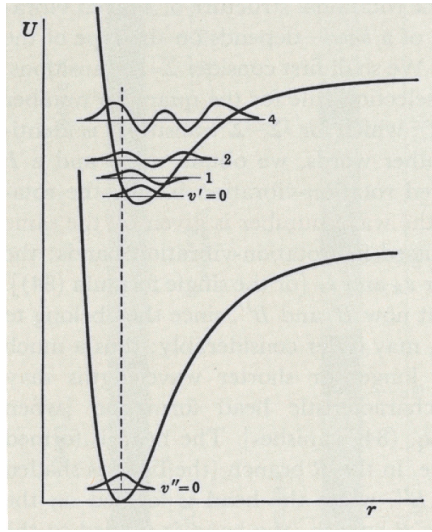

Figure 4.5: The diagram illustrates the Morse potentials of two electronic states with the eigenfunctions of the vibrational states. The best overlap for the state v" = 0 is with the state v' = 2 of the higher electronic state which is shown by the vertical dashed line. [22]

5

OH* Emission Spectra Model

The emission spectra of the OH^* radical is the main focus of the current project. The project requires the comparison of the experimentally obtained spectra with a model to understand its physical properties. In the current chapter the model developed to simulate the emission spectra from OH^* radical is discussed in detail. The model was developed in MATLAB for easy data processing. The choice was based on ease of use and relatively fast calculation speeds.

The steps described in the previous chapter are followed, where first the energy levels of the molecule are determined. Then the allowed transitions are selected based on the selection rules. Further the transition probabilities are calculated based on simple models with correction factors to account for the interaction between vibrational and rotational levels. The population distribution of the initial state is determined based on the vibrational and rotational temperatures. Lastly, based on the required output parameters the line shapes and line widths are adjusted. Finally the spectra from the developed OH^* model is compared with the widely used spectrographic tool LIFBASE to estimate the usability of the developed code.

5.1. Energy Levels & Allowed Transitions

The focus of the current project is on the ultraviolet radiation from the OH^* radical which is a result of the $A^2\Sigma \rightarrow X^2\Pi$ transition. Therefore the energy levels present in the first excited electronic state $A^2\Sigma$ and the ground electronic state $X^2\Pi$ need to be modelled. The rotational and vibrational energy expressions discussed in the previous chapter and the expressions with couplings constants from literature are used to describe the energy levels of the two electronic states. The values of the molecular spectroscopic constants are taken from the paper by Dieke and Crosswhite which is a standard paper for data on the OH^* radical [24].

The upper state is the $A^2\Sigma$ electronic state. As expressed by the molecular term symbol the state has a multiplicity of 2 which implies that spin splitting would exist. The resultant spin S of the state is $\frac{1}{2}$. It is a Σ state where the Hund's case (b) is most applicable. The rotational term value is defined by the equation 5.1 [24]. The last term in the expression R_v is the factor to account for the spin splitting. An average value of R_v is assumed in the model even though its value changes with the vibrational level.

$$\begin{aligned} F_1(v,N) &= B_{v,A}N(N+1) - D_{v,A}N^2(N+1)^2 + R_{v,A}\left(N+\frac{1}{2}\right) \\ F_2(v,N) &= B_{v,A}N(N+1) - D_{v,A}N^2(N+1)^2 - R_{v,A}\left(N+\frac{1}{2}\right) \end{aligned} \tag{5.1}$$

The lower state in the transition is the $X^2\Pi$ state. As mentioned in the previous chapter transitions are only allowed among states with the same multiplicity. Therefore even this state experiences spin splitting. The difference however is that it is a Π state. This implies that there exists Λ-doubling. In the current model the Λ-doubling is neglected as the difference in energy is negligible in comparison to the transition energies. Also based on the selection rule, transition is allowed only to one of the lambda doubled state from any particular state of the upper level. Also this state is an intermediate between Hund's case (a) and (b) therefore a coupling constant a is introduced into the rotational term value expression. This coupling constant a varies from $\pm\infty$ in Hund's case(a) to 0 in case (b). The equations for the rotational term expressions is given in equation 5.2

[24].

$$f_1(v,N) = B_{v,X}\left[(N+1)^2 - 1 - \frac{1}{2}\sqrt{4(N+1)^2 + a(a+4)}\right] - D_{v,X}N^2(N+1)^2$$
$$f_2(v,N) = B_{v,X}\left[N^2 - 1 + \frac{1}{2}\sqrt{4N^2 + a(a+4)}\right] - D_{v,X}N^2(N+1)^2 \tag{5.2}$$

The values of the rotational constants $B_{v,A}$ & $B_{v,X}$ and the centrifugal correction factors $D_{v,A}$ & $D_{v,X}$ are dependent on the vibrational quantum number. The correction factors $D_{v,A}$ & $D_{v,X}$ are assumed to be constant and an average value is chose. The rotational constants are expressed as per equation 5.3.

$$B_v = B_e - \alpha_e\left(v+\frac{1}{2}\right) + \gamma_e\left(v+\frac{1}{2}\right)^2 \tag{5.3}$$

where B_e are the equilibrium rotational constant and α_e & γ_e are the vibrational correction factors.

The vibrational levels for both the electronic states are expressed as per the simple equation 5.4 which was discussed in detail in the previous chapter.

$$G(v) = \omega_e\left(v+\frac{1}{2}\right) - \omega_e x_e\left(v+\frac{1}{2}\right)^2 \tag{5.4}$$

Finally the energy levels of the two electronic states in the term values is expressed as per equation 5.5.

$$T_A = T_{e,A} + G_A(v) + F(v,N)$$
$$T_X = T_{e,X} + G_x(v) + f(v,N) \tag{5.5}$$

The electronic energy of the lower ground state is assumed to be zero and all the energies are calculated from this reference. The values of all the spectroscopic constants used in the calculations of the energy levels are mentioned in table 5.1 which are sourced from the standard paper by Dieke and Crosswhite [24].

Spectroscopic Constant	**$A^2\Sigma$ state**	**$X^2\Pi$ state**
T_e	32682	0
ω_e	3184.28	3735.21
$\omega_e x_e$	97.84	82.21
B_e	17.355	18.871
α_e	0.807	0.714
γ_e	-0.00825	0.0035
D_v	$2.0525\text{x}10^{-3}$	$1.8367\text{x}10^{-3}$
R_v	0.103875	-
a	-	-7.547

Table 5.1: The spectroscopic constants for the OH^* radical. All the values are in the units of cm^{-1} which is commonly used in spectroscopy when using term values.

Using the given values, the model can be constructed to give the energy levels present in the two electronic states. After the different energy levels are obtained the transition energy would directly correspond to the difference in energy between the levels. As the energy is expressed in term values, a direct subtraction of the energies would provide the wavenumber for the transition.

Only particular transitions based on selection rules are allowed to occur. The selection rule on the total angular momentum J which is $\Delta J = 0, \pm 1$ needs to be strictly followed. The selection rule for Hund's case (b) on the quantum number N which is $\Delta N = 0, \pm 1$ doesn't need to be strictly followed. This is because the molecule behaves as an intermediate between case (a) and (b). However the transitions which follow the selection rule on ΔN would lead to stronger branches. The relation between the total angular momentum J and the quantum number N is the exclusion of spin angular momentum. The states F_1 & F_2 and f_1 & f_2 have a different spin leading to a different value of J for a particular value of N. The relation between the quantum numbers J and N for the different rotational states are expressed as follows.

$$F_1(N); f_1(N) : J = N + \frac{1}{2}$$
$$F_2(N); f_2(N) : J = N - \frac{1}{2}$$

Based on these selection rules, there exist 12 possible branches. The naming convention is based on ΔN with differences of *-2,-1,0,1,2* named *O,P,Q,R,S* respectively. The 12 branches are presented in table 5.2. The naming convention for the different branches is $X_{i,j}$ with X indicating ΔN, i identifying the upper rotational state and j indicating the lower rotational state. If only a single number is mentioned it implies that the number is repeated.

Branch	**Transition**	**ΔJ**
O_{12}	$F_1(N-2) \rightarrow f_2(N)$	-1
P_1	$F_1(N-1) \rightarrow f_1(N)$	-1
P_{12}	$F_1(N-1) \rightarrow f_2(N)$	0
P_2	$F_2(N-1) \rightarrow f_2(N)$	-1
Q_1	$F_1(N) \rightarrow f_1(N)$	0
Q_{12}	$F_1(N) \rightarrow f_2(N)$	1
Q_2	$F_2(N) \rightarrow f_2(N)$	0
Q_{21}	$F_2(N) \rightarrow f_1(N)$	-1
R_1	$F_1(N+1) \rightarrow f_1(N)$	1
R_2	$F_2(N+1) \rightarrow f_2(N)$	1
R_{21}	$F_2(N+1) \rightarrow f_1(N)$	0
S_{21}	$F_2(N+2) \rightarrow f_1(N)$	1

Table 5.2: This table shows the 12 branches present in the OH^* spectra along with the involved rotational level transition and the value of ΔJ of the transition.

5.2. Line Intensities

To obtain the spectra the intensity of emission from these possible transitions need to calculated. The intensity of a transition from state n to m is given by equation 5.6.

$$I_{nm} = N_n A_{nm} h\nu_{nm} \tag{5.6}$$

where N_n is the population of the state n, A_{nm} is the transition probability for that particular transition and ν_{nm} is the transition wavenumber. The transition wavenumber is obtained from the energy levels and the allowed transitions. The calculation of the transition probability and the population of states is discussed in the following sub-sections.

5.2.1. Transition Probabilities

In the current project the transition probability calculation formula is based on formulation from sources of Schadee and Mavrodineanu et. al. [12], [25]. The formula used in the current project is given in equation 5.7.

$$A_{nm} = C\frac{p_{J"}^{J'}}{2J'+1} k_{v"J"}^{v'J'} \nu_{nm}^3 \tag{5.7}$$

C is the constant proportionality factor which remains same for all the lines. As relative intensities are important this factor C can be eliminated. $p_{J"}^{J'}$ is the rotational transition probability from upper state J' to lower state $J"$. $k_{v"J"}^{v'J'}$ is the correction factor to include the relative intensities of different vibrational levels and the interaction between the vibrational and rotational levels. ν_{nm} is the transition wavenumber which is calculated from the transition energy difference.

The rotational transition probability $p_{J"}^{J'}$ is calculated based on the formula developed by Earls which are specific to $^2\Pi \rightarrow ^2\Sigma$ and $^2\Sigma \rightarrow ^2\Pi$ in diatomic molecules. In these transition probability formulas the statistical weight factor $(2J+1)$ is included which is divided in the transition probability expression. The gradual decoupling of the electronic spin from the inter-nuclear axis with increasing rotation is also taken into account. However the effect of Λ-doubling is neglected which is also neglected in the energy level calculation in the current project [24], [26]. The rotational transition probabilities are given as per the following equations.

R_2 S_{21}	$\frac{2J+1}{2J+2}\left((2J+1)\pm U\left[(2J+1)^2-2a\right]\right)$
R_1 Q_{12}	$\frac{2J+1}{2J+2}\left((2J+1)\pm U\left[(2J+1)^2+2(a-4)\right]\right)$
Q_2 R_{21}	$\frac{2J+1}{2J+2}\left(\frac{(2J+1)^2-2\pm U\left[(2J+1)^3-8J-2a\right]}{J}\right)$
Q_1 P_{12}	$\frac{2J+1}{2J+2}\left(\frac{(2J+1)^2-2\pm U\left[(2J+1)^3-8J+2(a-4)\right]}{J}\right)$
P_1 O_{12}	$\frac{2J+1}{2J}\left((2J+1)\pm U\left[(2J+1)^2-2a\right]\right)$
P_2 Q_{21}	$\frac{2J+1}{2J}\left((2J+1)\pm U\left[(2J+1)^2+2(a-4)\right]\right)$

where $U=\left[(2J+1)^2+a(a-4)\right]^{-\frac{1}{2}}$

In the presented equations the value of J are those of the $^2\Pi$ state. The equations are paired for the main branches and the satellite branches which have similar rotational transition probability expressions. The main branch is the branch on top and the satellite branch is lower. The difference in the expression is that wherever the '$\pm$ sign exists the + sign should be used for the main branch and $-$ sign for the satellite branch. Another change is that wherever the coupling constant 'a' is present, in the expression for the satellite branch it is replaced by $-(a-4)$. These equations predict the rotational transition probability for states $J>\frac{1}{2}$. For the states with $J=\frac{1}{2}$ the following rules 5.8 are applicable in the current case for the given branches. For branches not mentioned the probability is zero.

$$\begin{aligned} Q_2 = P_{12} &= \frac{16}{3} \\ R_2 = Q_{12} &= \frac{8}{3} \end{aligned} \tag{5.8}$$

The next part of the transition probability calculation is the term $k_{v"J"}^{v'J'}$. This term contains the relative intensity variation across the vibrational bands and also the vibration-rotation interaction factor. This factor is taken from the paper by Anketell and Learner who derive these factors from experimental measurements [27]. The factors are provided for vibrational levels of 0 to 4 for the upper and lower electronic state. The factors are provided for certain J values from $1\frac{1}{2}$ to $25\frac{1}{2}$ between which the factors are interpolated in the model.

5.2.2. Population of states

The population of the upper electronic state is necessary to determine the intensity of the line as given by equation 5.6. In the current model the population distribution of the molecule is assumed to follow the Boltzmann distribution. The Boltzmann distribution is valid when the molecule is in thermal equilibrium with the gas, vibrational and rotational temperature all being the same. The population fraction in any particular state is given by the Boltzmann distribution formula 5.9.

$$\frac{N(v,J)}{N_o} = \frac{e^{-\frac{E_v}{kT_{vib}}}\cdot(2J+1)\cdot e^{-\frac{E_r}{kT_{rot}}}}{Q_{vib}\cdot Q_{rot}} \tag{5.9}$$

E_v and E_r are the vibrational and rotational energies of the state respectively. T_{vib} and T_{rot} are the vibrational and rotational temperatures of the state. When in thermal equilibrium, both these temperatures are the same. In the current model there is a capability to adjust these temperatures separately. Q_{vib} and Q_{rot} are the vibrational and rotational partition functions respectively. The partition functions are given by the equations 5.10 which is the summation over all their respective states.

$$\begin{aligned} Q_{vib} &= \sum_v e^{-\frac{E_v}{kT_{vib}}} \\ Q_{rot} &= \sum_{v,J}(2J+1)\cdot e^{-\frac{E_r}{kT_{rot}}} \end{aligned} \tag{5.10}$$

5.3. Line Shape

There are various factors which lead to the broadening of spectral lines. The major factors for line broadening include the thermal motion of the molecules, collisions with other molecules and the natural line width based on the radiative lifetime of the molecule. These factors lead to Doppler broadening, Lorentz broadening and natural broadening. These line widths are visible only under very high resolution [12]. Apart from these natural broadening, the optical instrument used for measurement themselves have a certain '*instrument spectral response function*' which convolutes the various peaks in the spectrum. The instrument spectral response function is also known as 'apparatus function' or simply 'instrument function'. This convolution is based on the optical properties of the various optical tools (lenses,grating,slits) in the spectrometer. In the current project the apparatus function of the spectrometer is much higher then the physical broadening phenomenon.

For the current model the line width and shape doesn't take into account the physical broadening phenomenon but directly applies a convolution based on a given apparatus function. The line shape chosen for the convolution is a Voigt profile. The Voigt profile is a convolution of a Gaussian profile and a Lorentzian profile. This line shape is widely used to model spectrum as they contain both these profiles[28]. The Voigt profile is computational heavy due to the integral required for a perfect convolution. To save on computation, in the current project a pseudo-Voigt profile is used which is a linear combination of a Gaussian and Lorentzian profiles based on equation 5.11.

$$V(x) = \eta \cdot L(x,\gamma) + (1-\eta) \cdot G(x,\sigma) \tag{5.11}$$

The Gaussian and Lorentzian profiles are given by equations 5.13.

$$L(x,\gamma) = \frac{\gamma}{\pi\left[(x-x_o)^2+\gamma^2\right]} \tag{5.12}$$

$$G(x,\sigma) = \frac{1}{\sigma\sqrt{2\pi}} e^{-\frac{(x-x_0^2)}{2\sigma^2}} \tag{5.13}$$

The full width half maximum (FWHM) for these profiles are given by the equations 5.15.

$$f_L = 2\gamma \tag{5.14}$$

$$f_G = 2\sigma\sqrt{2ln(2)} \tag{5.15}$$

The relation between the FWHM of the Voigt profile f_V, the FWHM of the Lorentzian profile f_L and the linear combination factor η is given by equation 5.16 [29]. This relation approximates the pseudo-Voigt profile to the actual Voigt profile with a maximum deviation of 1.2%.

$$\eta = 1.36603(f_L/f_V) - 0.47719(f_L/f_V)^2 + 0.11116(f_L/f_V)^3 \tag{5.16}$$

To complete the set of equations to construct the profile a relation between all the FWHM's of all the profiles is necessary. This is given by equation 5.17 [30].

$$f_V = 0.5346 f_L + 0.5\sqrt{0.86639 f_L^2 + 4 f_G^2} \tag{5.17}$$

With all the given relations the spectra can be constructed given an input of the linear combination factor η and the apparatus function which is same as the FWHM of the Voigt profile f_V. Using equation 5.16 the FWHM of the Lorentzian profile can be estimated. Then the equation 5.17 is used to calculate the FWHM of the Gaussian profile f_G. The defining parameters σ and γ can be estimated from the FWHM relations 5.15. The Gaussian and Lorentzian profiles can be constructed and added as per equations 5.13 and 5.11 to get the complete line shape. This procedure is applied to all the lines in the wavelength range of choice to obtain the spectra.

5.4. Summary and Comparison

In the current section the overall characteristics of the model are highlighted briefly to provide an overall picture. The assumptions made in the model are touched upon. The required input to generate a spectrum are also listed. Finally the output simulated spectra is compared with a widely used spectroscopic tool LIFBASE [31].

Assumptions

- **Λ-Doubling** - The splitting of states in the $^2\Pi$ ground state due to Λ-doubling is neglected. The difference in energy between the levels is assumed to be very small as compared to overall transition energy.
- **Centrifugal correction factor D_v** - The difference in values between the values of D_v across vibrational levels is assumed to be small. The overall effect on the transition energy is very small so an average constant value is chosen.
- **Population of states** - A thermalised population distribution based on the Boltzmann distribution is assumed for the $A^2\Sigma$ state based on the given vibrational and rotational temperatures. The assumption implies that thermal equilibrium exists within the vibrational and rotational levels. If both these temperatures are assumed the same then it also implies that thermal equilibrium exists in the gas.
- **Line shape** - The convolution of the apparatus function should be made after the line broadening due to physical phenomenon is taken into account. In the current model, the apparatus function is directly applied to the line spectrum. Also the shape of the apparatus function is assumed to be a Voigt profile which is further model by a psuedo-Voigt formulation for computational efficiency.

Inputs

- **Temperatures** - The vibrational (T_{vib}) and rotational temperature (T_{rot}) can be taken the same or they can be individually varied based on the requirement.
- **Voigt linear combination factor (η)** - The amount of Lorentzian and Gaussian portion of the Voigt profile can be varied.
- **Apparatus function (f_V)** - The apparatus function which is the FWHM of the Voigt profile can also be chosen and varied as per the requirement in the experimental setup.

Output

The final output is the simulated spectra from all the calculations. An example is presented in figure 5.1. This spectra is in the ranges of 275 nm to 340 nm. The apparatus function (f_V) is 0.5 nm with the factor η set to 0.5. The vibrational and rotational temperatures are given as 3000 K.

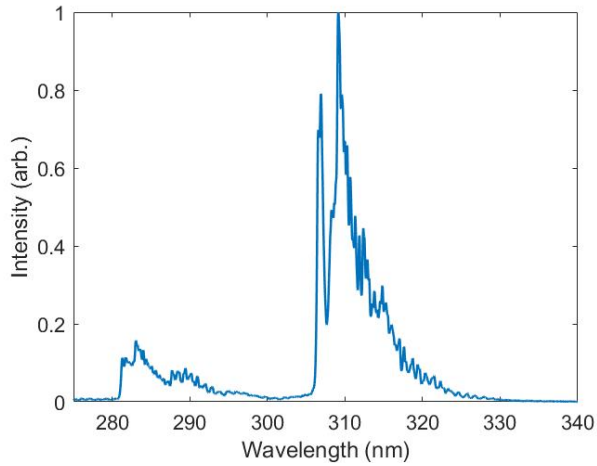

Figure 5.1: Simulated spectra of the OH^* radical from the $A^2\Sigma \rightarrow X^2\Pi$ transition in the limits 275 to 340 nm. Parameters: $f_V = 0.5nm$, $\eta = 0.5$ & $T_{vib} = T_{rot} = 3000K$.

In the figure we see two distinct regions with lines. The region from 280 to 300 nm consist of lines from vibrational bands with $\Delta v = 1$ and the region of 305 to 330 nm consists of lines from the vibrational bands with $\Delta v = 0$. For the current project we focus on the spectrum from 305 nm to 320 nm in the experiments due to limitations in the sensitivity of the camera.

Comparison

In the current section the created model is compared against the commonly used spectroscopic tool LIFBASE. In the figure 5.2 both the models are shown in the same plot in the wavelength range of 305 nm to 320 nm. The spectra generated are for pure Gaussian line shape (η=0) with the apparatus function of 0.2 nm. The temperature for which the spectra are generated is 3000 K with the vibrational and rotational temperatures assumed to be the same.

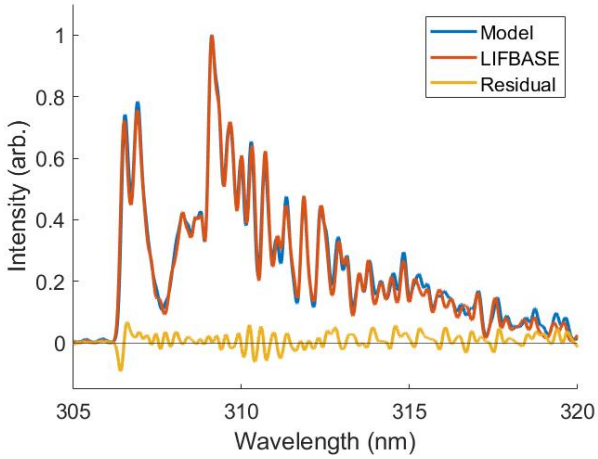

Figure 5.2: The constructed model is compared with the model from the spectroscopic tool LIFBASE. The blue line shows the constructed model and the red line is the spectra from LIFBASE.

This comparison doesn't validate the model entirely but shows how close the generated model in the current project is to the spectroscopic tools which are widely used in industry. The constructed model does provide an exact fit. Some of the peaks do match the LIFBASE model exactly. They vary in intensity by a small margin at some of the peaks with a maximum difference of around 3% in intensity. In the region of 315 nm to 320 nm which correspond to lines with high J values, the line position also has a slight difference with a maximum variation of 0.05 nm.

6

Experimental Setup

After the model has been developed, an experimental measurement is necessary to compare the modelled and experimental observation. An experimental setup has been built as part of the project to capture OH^* spectrum in flames for the wavelength range of 300 nm to 330 nm.

6.1. Setup

The experimental setup consists of two distinct parts - the flame and the spectrometer.

Flame

The experiment captures the spectra from a laminar premixed CH_4/air flame. The gases come from pressurised cylinders whose pressure is brought down to atmospheric pressure through valves. The volumetric flow rate of the gases is controlled through rotameters. The required equivalence ratio for the flame is set based on the volumetric flow rates and the density of the gases. A Bunsen burner is used to hold the flame. A v-shaped flame is generated by introducing a thin metal rod near the mouth of the burner.

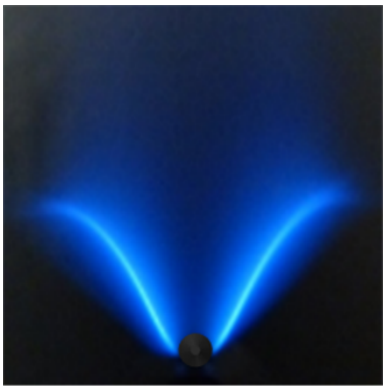

Figure 6.1: A picture of a v-shaped flame stabilised on a metal rod over a Bunsen burner.

A v-shaped flame is stable for a narrow range of flow rates. The purpose of using a v-shaped flame was to reduce a 3-D conical flame into a 2-D flame. This reduces the integration of light in the light path from different regions of a flame. Another advantage of a v-shaped flame is the increase in captured light intensity. The light emitting flame front is reduced to 2-D from 3-D which allows for better integration of light in the direction of light capture. This is better illustrated through figure 6.2 which shows the difference in light integration along the line of sight between a conical flame and a v-shaped flame.

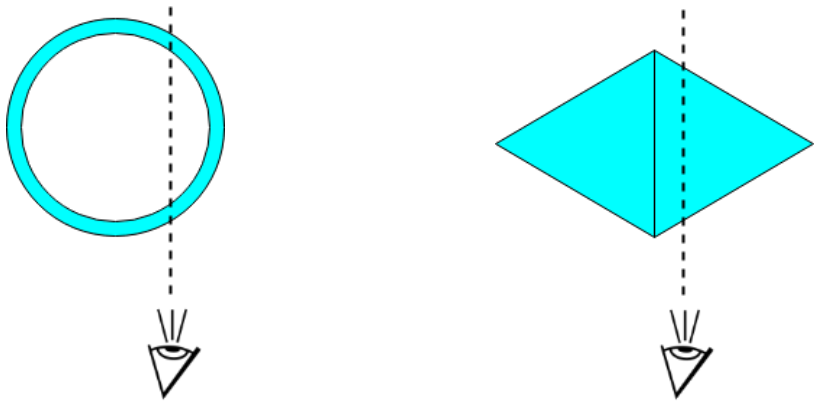

(a) The line of sight path for a conical flame

(b) The line of sight path for a v-shaped flame

Figure 6.2: The difference in the light integration along line of sight between a conical flame and a v-shaped flame

Spectrometer

The next part of the experimental setup is the spectrometer which captures the spectra from the flame. The spectrometer consists of lenses to direct the light in the required direction, a grating to disperse the different wavelengths and an image sensor to capture the light. The schematics of the spectrometer setup are presented in figures 6.3 and 6.4.

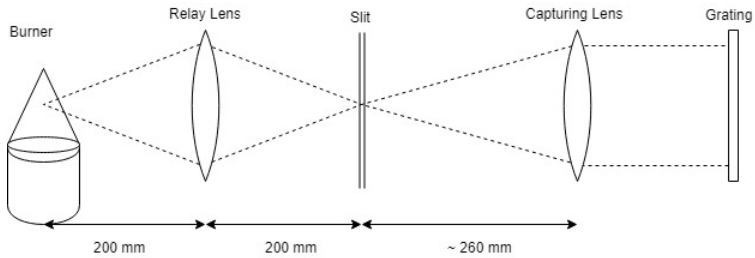

Figure 6.3: A schematic of the spectrometer setup from the side view. The side view contains only a portion of the setup as the focusing lens and camera are obstructed from view.

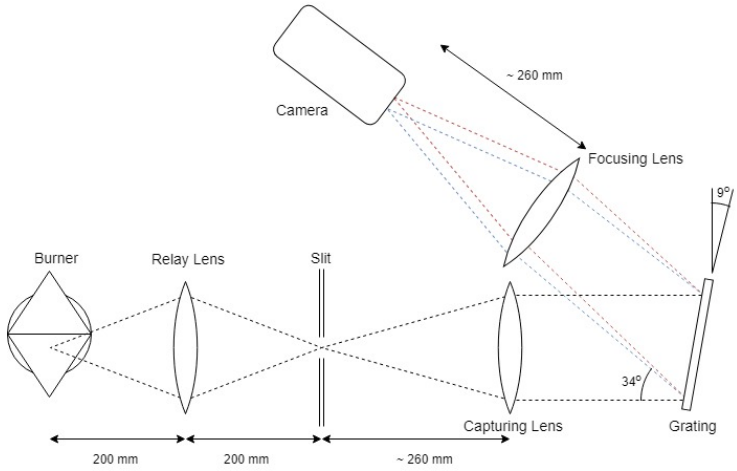

Figure 6.4: A schematic of the spectrometer setup from the top view.

The components of the spectrometer are discussed in detail.

- **Lenses** - The lenses used in the setup are made of UV-grade fused silica. The material of the lens is an important factor as most common lenses manufacture for the visible range have very low transmittance in the UV- range. The lenses used in the setup are 50.8 mm in diameter except for the relay lens which is 75 mm. All the lenses are spherical plano-convex lenses. The relay lens has a focal length of 100mm and acts as a 2F relay. This lens generates an inverted image of the flame at the plane of the slit. The capturing lens and focusing lens are a lens system of two lenses each. The lens system consists of 2 lenses with a 500 mm focal length placed close to each other to give a combined to focal length of around 260 mm.

- **Slit** - The slit is used to allow the light from only a certain portion of the flame to pass through. In the spectrometer setup a 200 μm slit was used for the flame spectra measurements. The disadvantage of using a slit is that it allows light to pass through which does not originate from the location in focus. Using a pinhole in the place of a slit would minimise this cross contamination of light. This is illustrated in figures 6.5 and 6.6.

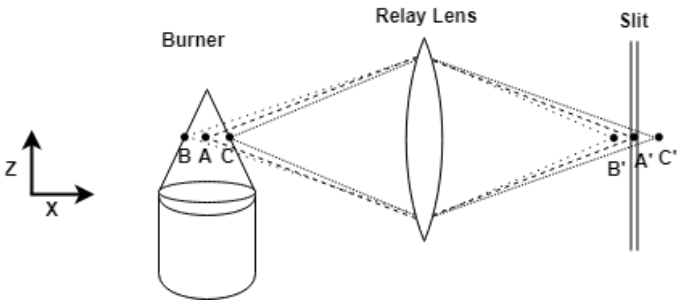

Figure 6.5: The diagram shows the side view of the setup with the light rays emanating from different locations in the X-Z plane. In this plane, the light rays are not blocked by the slit and are allowed to pass through.

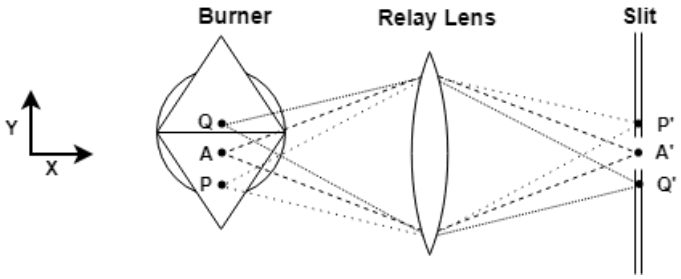

Figure 6.6: The diagram shows the top view of the setup with the light rays emanating from different locations in the X-Y plane. In this plane, the light rays are allowed only from a particular point in the X-Y plane.

The figures show that light from a single X-Z plane is imaged. The image in focus would be from an X distance of 200 mm. However the slit does not block light from other points in the X-Z plane which would interfere with the image quality.

- **Grating** - The grating is used to disperse the different wavelengths spatially. The grating used is a 400 nm blaze wavelength reflective diffraction grating. It has 1200 grooves per mm which is the inverse of the groove spacing. The advantage of using a low groove spacing provides a higher angular dispersion. The efficiency of the grating at 300 nm is around 55% [32]. The grating is mounted on an angular stage which can be rotated for easier wavelength selection. To calibrate the angles used in the grating, a few tests were done using a 400 W UV-B emitting mercury lamp. The lamp was coated to not allow strong UV lines but contained a strong signal from mercury lines at 365 nm and 405 nm. These lines were used to calibrate the angular stage. The signal captured from the mercury lamp is shown in figure 6.7. The

angles on the angular stage were noted for the 365.02 nm, 404.66 nm and 407.78 nm peaks when these peaks were centred on the image sensor. These wavelengths and angles were utilised to back calculate the grating angle required for a signal at 306.4 nm in the case of OH^* spectra.

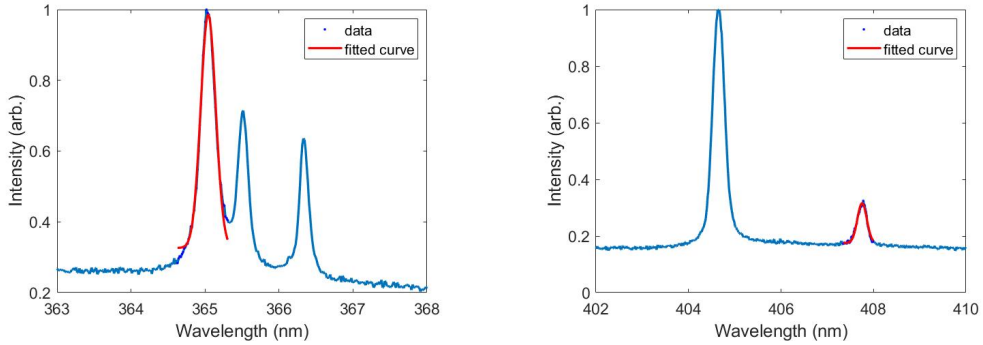

(a) The 365 nm peaks of the Hg spectrum with the peak at 365.02 nm fitted with a Gaussian to mark the exact location.

(b) The 405 nm peaks of the Hg spectrum with the peak at 407.78 nm fitted with a Gaussian to mark the exact location.

Figure 6.7: The spectrum from a mercury lamp used to calibrate the angular stage of the grating

- **Image Sensor** - The camera used in the spectrometer is a front illuminated scientific-CMOS (sCMOS) sensor which is a CMOS sensor optimised for scientific applications. The sensor is 2048x2048 pixels with a pixel size of 6.5 μm. The quantum efficiency of the camera varies as per the curve given in figure 6.8. The efficiency varies from 5.5 % to 15 % in the wavelength range from 300 nm to 340 nm respectively [33].

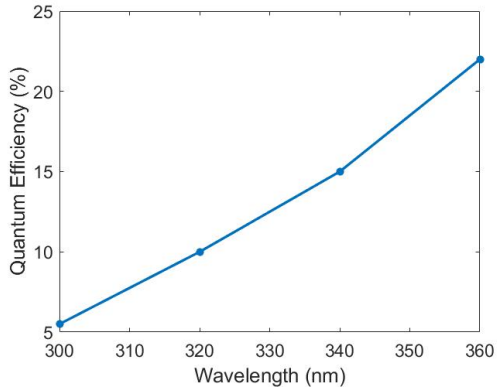

Figure 6.8: The plot of the quantum efficiency variation of the camera sensor as a function of wavelength

6.2. Output & Post-processing

The spectrometer setup captures the photons of different wavelengths coming from the flame. The measurements taken for the flame studies consist of 5 shots taken with an exposure time of 10 seconds each. The high exposure time is to have a good signal to noise ratio at the low sensitivity of the camera. The image is also digitally binned. Binning implies intensity of a pixel is binned with its neighbouring pixels. In the current measurements an 8x1 binning is used. This implies that 8 pixels in the vertical direction are binned. The pixels are not binned horizontally because this would decrease the resolution of the spectrum. The output image on the camera and the final spectra are presented in figures 6.9a and 6.9b.

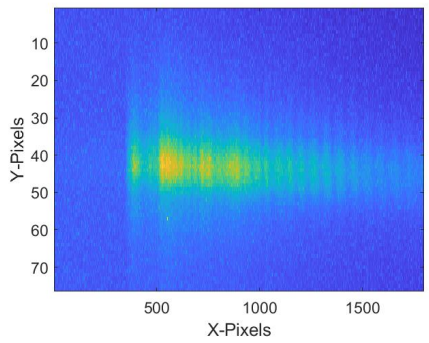

(a) The single shot raw image captured by the camera with an exposure time of 10 seconds

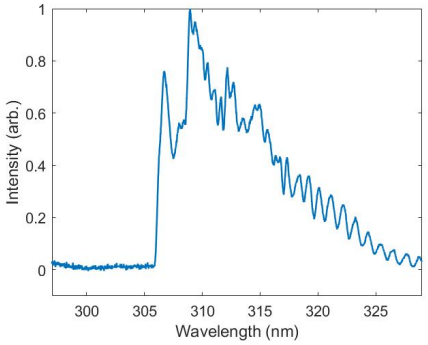

(b) The final spectrum obtained all the steps of post-processing

Figure 6.9: The diagrams showing the captured raw image and the post processed spectrum which is extracted from the image.

The image captured on the camera needs to be processed before a spectra is obtained. The conversion of the raw image into an OH^* spectra is done through the following steps in the current project. The need for each of the step in the post-processing is discussed. The flow chart of images for the conversion of the raw image into the final spectrum is presented in figure 6.10.

1. **Shot averaging** - The spectra is made from averaging 5 shots. The process of averaging helps in reducing the impact of spurious errors. It also improves the signal to noise ratio of the spectra.

2. **Background subtraction** - After averaging 5 shots of the signal image, the averaged signal image is subtracted with an averaged background image. The background image is taken by covering the slit and taking an image. This background shot subtraction eliminates light reflected from other surfaces in the lab and not originating from the slit. It also helps in eliminating dead pixels if any in the camera sensor.

3. **ROI selection** - The signal is confined to a portion of the sensor. This region of interest (ROI) of the sensor is selected and used further to generate the spectrum.

4. **Bowing effect correction** - The spectrometer consists of an error in imaging a slit. The straight slit is imaged as a curve when it undergoes diffraction through a grating [34]. This curvature needs to be accounted for before averaging the values of the pixels vertically. In the post processing the curvature in the image is corrected by shifting the pixels to remove the curvature.

5. **Average line plot** - After correcting for the curvature of the image, The vertical pixels in the ROI are averaged to form a single line plot across the horizontal axis which is the wavelength axis.

6. **Camera efficiency correction** - This spectrum generated needs to be corrected for the quantum efficiency variation of the camera sensor with respect to the wavelength of light observed. This correction is based on the values from figure 6.8. The correction is done by considering 2 linear variations in efficiency. The 2 sections are from 300 nm to 320 nm and 320 nm to 340 nm. A linear correction is applied based on interpolated values of the camera efficiency.

7. CO_2^* **continuum correction** - The spectrum captured from the flame contains contributions from the OH^* radical as well as the CO_2^* molecule in the wavelength range of 300 nm to 330 nm. This is also seen in the figure 2.3 from the Combustion chapter. The contribution from CO_2^* needs to be subtracted to isolate the OH^* spectrum. The spectrum from CO_2^* exists as a continuum which adds to the intensity at all wavelengths. In the current project the variation of the CO_2^* continuum is assumed to be linear in the wavelength range of 300 nm to 320 nm. The underlying slope in the spectrum observed is attributed to CO_2^* and is removed to obtain the final OH^* spectrum.

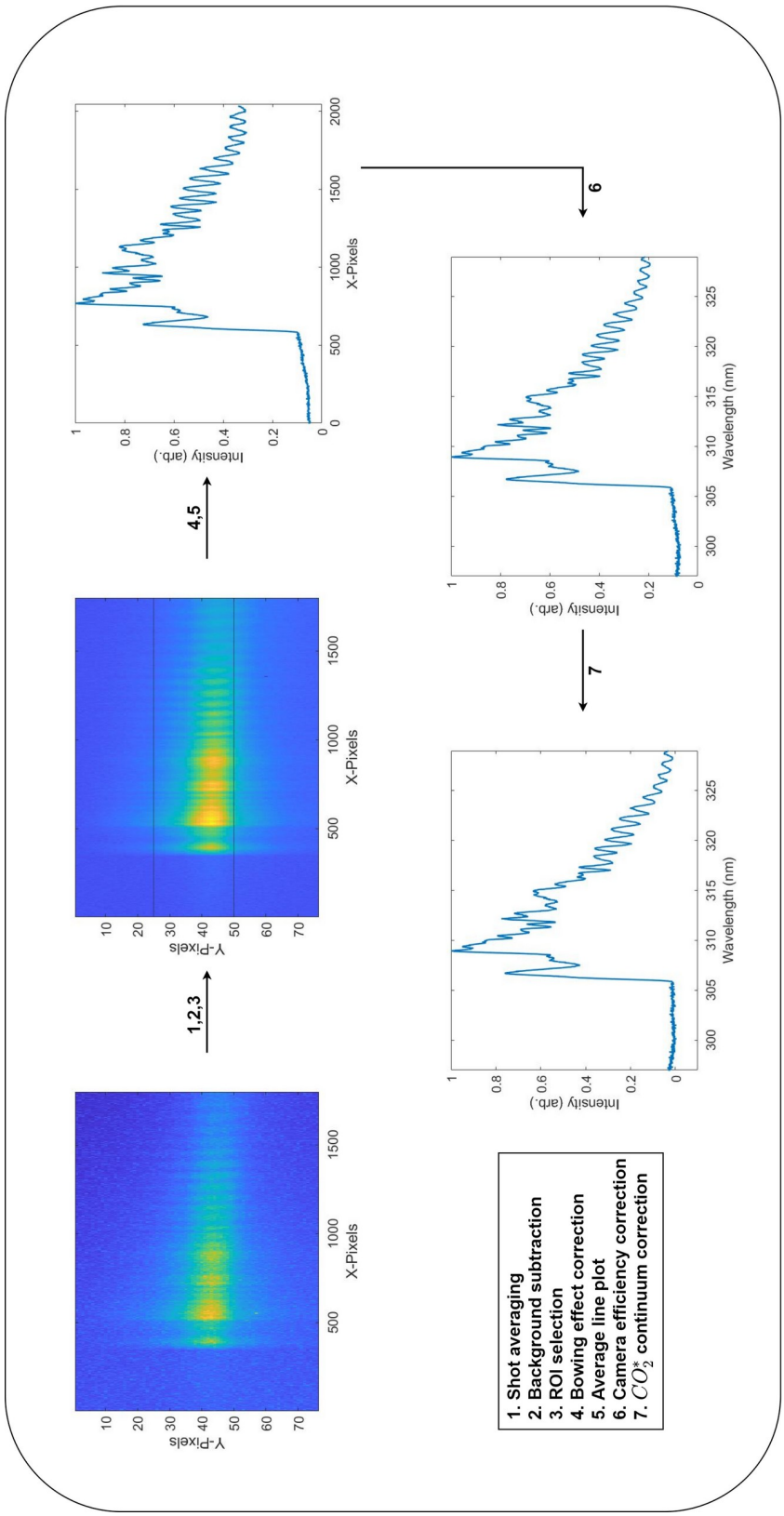

Figure 6.10: The flow chart showing the different stages in the post processing with the operations done listed.

7

Results and Discussion

In the current chapter the results are presented from the experimental studies conducted on the flame spectra. The goal of this section of the project is to gain temperature information from the OH^* spectra captured from flames. This would help in determining the feasibility of using OH^* spectra in practical combustors for thermometry. To obtain spectra from flames at different temperatures two different studies are chosen. The temperature of the flame is different for different equivalence ratios. Another temperature variation which can be studied is the variation of temperature across a flame front. These two studies are discussed in detail.

7.1. Spectrum fitting

An important step in determining the temperature of the flame is the comparison of experimental spectrum with a simulated spectrum. The procedure followed in the project is to find a best fit for the experimental spectrum. As mentioned in chapter 5, the model requires three input parameters temperature, η and f_V. There parameters are also the variables allowed to vary for the best fit search. An optimisation for speed and resolution needs to be decided for an effective best fit algorithm. As the resolution of the search is improved the a better fit can be obtained but this would also take a higher time to search for the best spectrum fit. The step sizes used in the search for the studies in the project are given in the table 7.1 along with the bounds within which the search algorithm functions.

Parameter	Step Size	Bounds
T_{rot}, T_{vib}	100 K	1500 K - 10000 K
η	0.05	0 - 1
f_V	0.05 nm	0.2 nm - 1 nm

Table 7.1: The step sizes and bounds used in the search for the best spectrum fit.

The best fit is obtained by comparing an error value for all the spectra in the search space. A least square error is calculated at all the points on the wavelength axis comparing the experimental spectrum with the simulated spectrum. The summation of the least square error values along the wavelength axis provides an error value for the fit. The best fit spectrum is the one with the least error value.

7.2. Variation with equivalence ratio

The first study is the study of spectra from flames with different equivalence ratios. The gas temperature is different at different equivalence ratios which would theoretically provide OH^* spectra at different temperatures.

7.2.1. Measurement parameters

The measurements are taken from a v-flame at different equivalence ratio by adjusting the volumetric flow rates of CH_4 and air. The equivalence ratios are varied from 0.8 to 1.2 in steps of 0.1. The total flow rate for the operation of the Bunsen burner is held constant at 8 SLPM (standard litres per minute). As per this flow

rate and pipe dimensions the Reynolds number comes out to around 1000 where laminar flow is expected. The flame spectrum is gathered from a vertical slice close to the base of the v-shaped flame. The location is marked in figure 7.1.

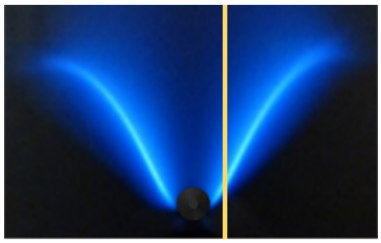

Figure 7.1: The v-shaped flame marked with the location of the imaged slit. The size of the slit is exaggerated for a clear visual.

The spectrum at each equivalence ratio was generated from 5 images which are taken with an exposure time of 10 seconds each. Also, 5 background shots are taken by covering the slit with the same exposure time.

7.2.2. Results

The temperature analysis of the obtained spectra are done by a least square error fit with the spectra simulated by the model. The parameters which are allowed to vary are the Voigt linear combination factor (η), Apparatus function (f_V) and the temperature. There are two temperature fit case studies done within each of the study. In '*case study 1*' the rotational and vibrational temperatures are assumed to be the same. In '*case study 2*' the rotational and vibrational temperatures can vary independently. The temperature fit case studies have 4 sub-cases. These 4 sub-cases correspond to the wavelength ranges over which the spectrum fitting routine is run. The sub-cases are given in table 7.2.

Sub-case	Wavelength Range
A	305 nm - 320 nm
B	305 nm - 312 nm
C	312 nm - 320 nm
D	308 nm - 320 nm

Table 7.2: The wavelength ranges chosen for the least square error spectrum fitting routine to determine the temperatures involved

These wavelength ranges are selected based on the location of the various peaks from the (0-0) and (1-1) vibrational bands. The major peaks present in the spectrum in the wavelength range captured in the experiment is shown in figure 7.2. The peaks refer to the final convoluted shape of the most intense lines of a particular rotational branch. The figure is generated in LIFBASE with important peaks marked.

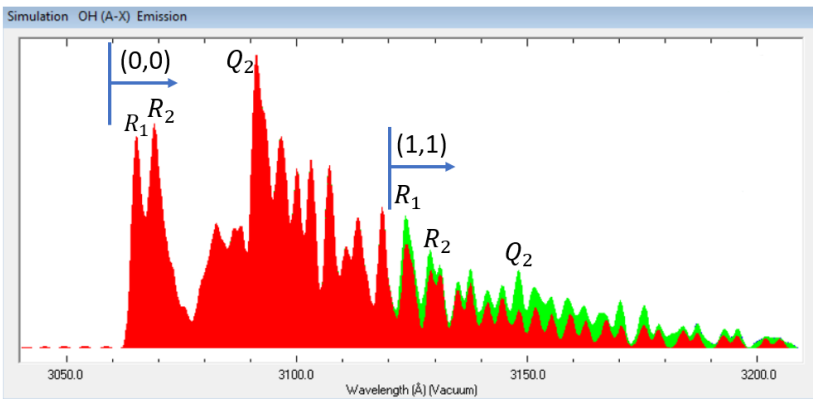

Figure 7.2: The contributions from the different vibrational bands is marked with different colours. The locations of a few important branches are also marked. [31]

The figure 7.2 shows the contribution to the spectra from different vibrational bands in different colours. The red portion corresponds to the contribution from the (0-0) vibrational band and the green region is the contribution from the (1-1) vibrational band. The sub-cases are chosen such that these contributions can be differentiated. The sub-case A takes into consideration the entire wavelength range. The sub-case B only uses the portion of the spectrum with contribution from the (0-0) vibrational band. The sub-case C consists of the portion of the spectrum with contributions from both the bands. The sub-case D is used in the case study where rotational and vibrational temperature are allowed to vary. This implies that a region with contribution from both is necessary. The first few peaks were eliminated from the complete wavelength range to obtain this wavelength range. This range was chosen based on experience from the spectrum fits. It was observed that the intensity of the R_1 and R_2 peaks in the (0-0) vibrational band are much lower then the simulated spectrum peak intensities. This skews the normalisation of the spectrum leading to bad spectrum fits. Hence these peaks were eliminated and a wavelength region of 308 nm - 320 nm was chosen.

Case Study 1

In this case study, $T = T_{rot} = T_{vib}$ is assumed. An example of the best spectrum fit result in presented in figure 7.3. The shown example is for the spectrum from a flame of $\phi = 1.0$ analysed as per the limits of sub-case A. The best fit temperature for this case is 6400 K.

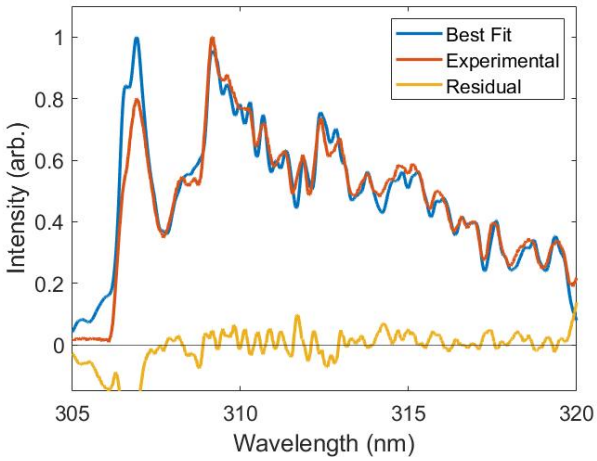

Figure 7.3: The spectrum fit of the experimental spectra with the simulated spectra of the best fit. The case shown is for $\phi = 1$ with the wavelength range of sub-case A.

The sub-cases A,B and C are analysed in this case study. The result of the spectrum fits are presented in figures 7.4a, 7.4b and 7.5.

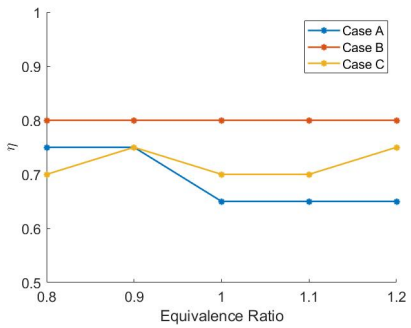

(a) The variation of the Voigt linear combination factor η with equivalence ratio

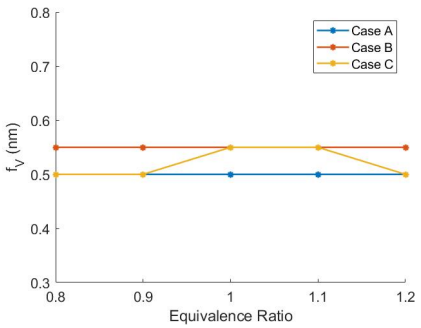

(b) The variation of the apparatus function f_V with equivalence ratio

Figure 7.4: The variation of η and f_V with the equivalence ratio.

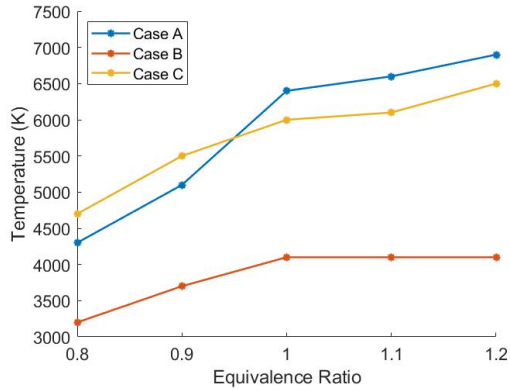

Figure 7.5: The variation of the best fit temperatures for the sub-cases A, B and C as a function of equivalence ratio

From figure 7.3 it can be observed the best fit spectrum provides a relatively good match apart from the R_1 and R_2 peaks of the (0-0) band. This was the reason given for the choice of wavelength range of sub-case D. The residual from the spectrum fits is fairly small and this provides a good confidence in the fits obtained by the search algorithm.

The figure 7.4a shows a variation of η between the values of 0.65 to 0.8. The line shape is not fairly constant but no particular trend is observed. The apparatus function f_V remains fairly constant as seen in figure 7.4b. The variation observed is only for sub-case C which is also only by 0.05 nm.

The figure 7.5 shows the variation of the temperature obtained from the spectrum fits. An increasing trend with equivalence ratio is observed for sub-cases A and C. For sub-case B the temperature increases upto stoichiometric conditions but remains constant at 4100 K for higher equivalence ratios. The values of the temperatures for sub-case B is much lower as compared to sub-cases A and C which have temperatures in the same range. The temperature values are tabulated in appendix A.

Case Study 2

For case study 2, the values obtained for η and f_V from case study 1 are directly utilised. This is because these parameters would remain relatively constant with changes in temperature. The parameters which can vary are T_{vib} and T_{rot} with a step size of 100 K. The sub case D is chosen for this analysis. The vibrational and rotational temperatures obtained are presented in figure 7.6

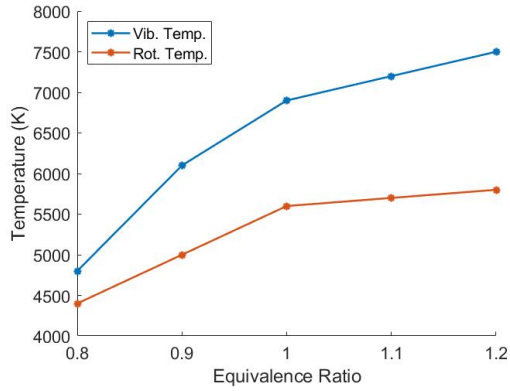

Figure 7.6: The variation of the obtained rotational and vibrational temperatures as a function of equivalence ratio. The spectrum fit was done on the wavelength range of sub-case D.

It is seen from figure 7.6 that the vibrational and rotational temperatures obtained from the spectrum fits are very different. The rotational temperatures are lower than the vibrational temperatures. The trend observed for both these temperatures is that they increase as a function of the equivalence ratio. The slope

of the vibrational temperature curve is much higher as compared to the trend of the rotational temperature curve. The temperature values are tabulated in appendix A.

7.2.3. Discussion

When a simple equilibrium study is considered, the temperature at different equivalence ratios is based on the heat capacity of the products and the reactants present in the flame. In reality the chemical kinetics also play a role in determining the gas temperature of the flame. The theoretical flame temperature is estimated using CHEM1D which is a one-dimensional reactive flow solver [4]. The actual temperature of the gas would be below the adiabatic flame temperature as there exists heat loss from the system. The variation of the adiabatic flame temperature with the equivalence ratio is presented in figure 7.7.

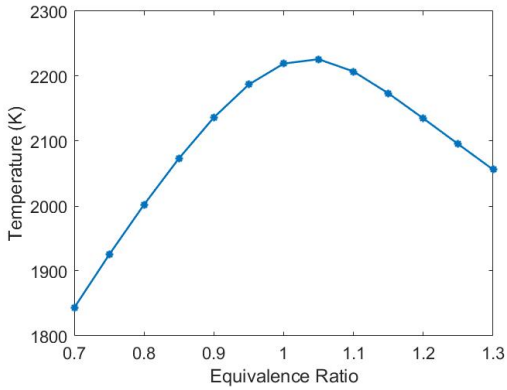

Figure 7.7: The variation of the adiabatic flame temperature with equivalence ratio calculated using CHEM1D

It is observed that the expected temperature variation is between 2000 K to 2200 K. The temperatures obtained from the spectra however are much higher. The shape of the variation is also not as per the expected curve where a maximum is seen close to the stoichiometric condition. There is however a difference in the slope of the curve on the lean and rich side of the flame. In case study 1, the temperature in sub-case A varies from 4300 K to 6900 K. An interesting observation is the difference in temperatures obtained from sub-case B as compared to sub-cases A and C. The sub-case B contains information only from the (0-0) vibrational band which shows a much different temperature variation which is still not close to the adiabatic flame temperatures. This points to a disparity in the assumption that the different vibrational and rotational levels are populated as per the Boltzmann distribution. This is further proved in case study 2.

In case study 2 where the rotational and vibrational temperatures are allowed to vary, the two temperatures predicted are not the same and have a significant difference. If thermal equilibrium exists in the system the two temperatures would be the same. The vibrational temperatures predicted are much higher which point to a higher population in higher vibrational states as compared to a system in thermal equilibrium. The rotational temperature measured at the stoichiometric condition is 5600 K which is relatively close to the value of 5200 K obtained by Broida [35]. The OH^* radical has a radiative lifetime of 10^{-6} seconds in which time it undergoes around 10^4 collisions. These collisions are insufficient to bring the population to a thermal equilibrium as per the observed spectrum.

Even though the temperatures obtained are not the gas temperatures in the flame, the temperatures fit provide a unique mapping to the equivalence ratio in the flame. If the system is calibrated accordingly such a technique can be utilised to measure the equivalence ratio in the flames even with the disparity due to non-thermal behaviour of the spectrum.

7.3. Variation across the flame front

There exists a temperature variation across the flame front. This study consists of testing if a variation in temperature can be seen through the OH^* spectrum.

7.3.1. Pseudo-spatial resolution

Before obtaining the spectrum from different sections of the flame. An estimation needs to be made to determine the spatial resolution of the spectrometer. In the current project the actual spatial resolution is not measured but a pseudo estimate is obtained for the current measurement technique. A razor is placed across the slit to block a portion of the spectrum. The sharpness of the razor edge on the imaging plane is quantified. The line spread function from the razor edge is used to define the pseudo-spatial resolution. The actual spatial resolution of the system needs to be quantified based imaging the sharpness of an image from the object plane but in this case the resolution is estimated from an image at the plane of the slit.

The portion of the image used to estimate the pseudo-spatial resolution is shown in figure 7.8.

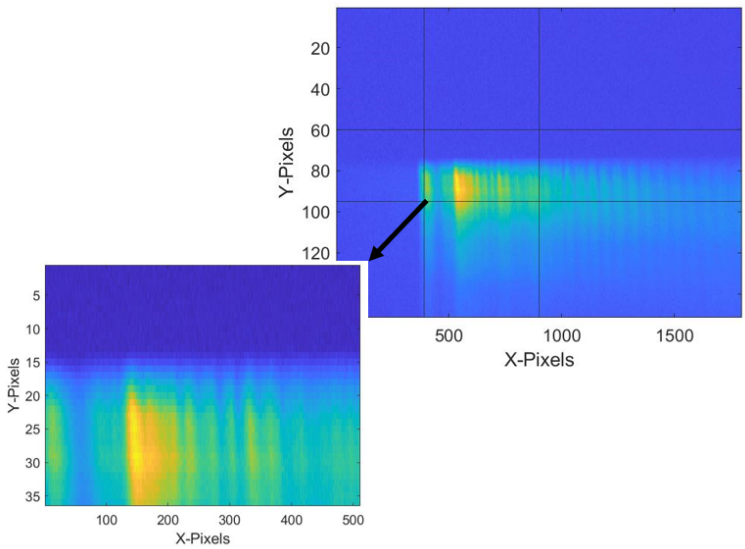

Figure 7.8: The selected portion of the signal used to calculate the pseudo-spatial resolution of the spectrometer

From the selected portion of the image the following operations are carried out to determine the resolution. The edge spread function for an array of data is given by the equation 7.1.

$$ESF = \frac{X - \mu}{\sigma} \tag{7.1}$$

where X is the array of intensity data, μ is the average of the intensity data in the array and σ is the standard deviation of the intensity data. Then the formula for the edge spread function is applied to each of the vertical arrays in the ROI. This edge spread function of all these arrays are averaged to obtain an average edge spread function. The line spread function is simply the first derivative of the edge spread function given by equation 7.2.The FWHM of the Gaussian fitted to the LSF determines the resolution.

$$LSF = \frac{d}{dx}(ESF) \tag{7.2}$$

The ESF and LSF calculations based on the selected ROI is shown in figures 7.9a and 7.9b respectively.

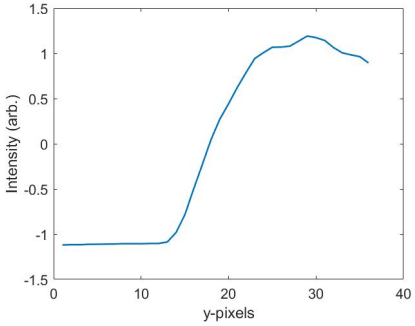

(a) The edge spread function (ESF) obtained from the processing of the image

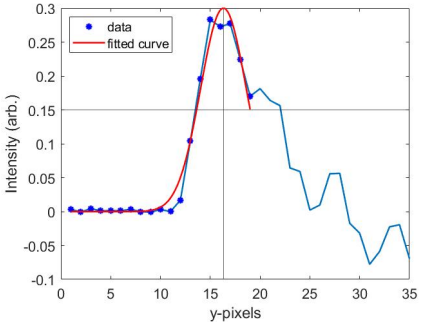

(b) The line spread function (LSF) obtained from the processing of the image. There is also a Gaussian curve fit on the LSF to obtain the FWHM of the curve which determines the resolution.

Figure 7.9: The diagrams show the edge spread function and the line spread function which are used to determine the pseudo-spatial resolution of the system.

It is important to remember that each of the vertical pixel is a binned pixel of 8 individual pixels. Also the individual pixels have a size of 6.5 μm. The calculation of the pseudo-spatial resolution is as follows.

$$
\begin{aligned}
& FWHM \approx 5\ binned\ pixels \\
\Rightarrow\ & FWHM \approx 43\ pixels \\
\Rightarrow\ & FWHM \approx 280\ \mu m
\end{aligned}
$$

This implies that the pseudo-spatial resolution of the system is around 280 μm. This also points to the minimum range of binned pixels which can be chosen as the ROI to generate a spectrum.

7.3.2. Measurement parameters

Even this study utilises a laminar premixed CH_4/air v-shaped flame over a Bunsen burner. The flame is at stoichiometric condition with a total flow rate of 8 SLPM. The v-flame is however tilted at an angle such that one of the 2-D flame planes is horizontal in the imaging plane. The purpose of using a horizontal flame is to ensure that the portion imaged from the slit, images the flame across the flame front from a similar portion of the flame. The figure 7.10 shows the tilted v-shaped flame used in the measurements along with the portion chosen with the slit.

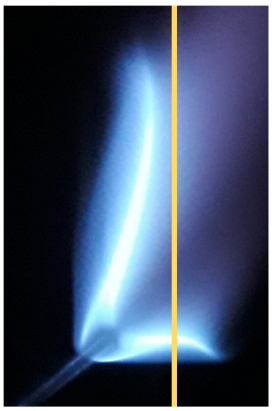

Figure 7.10: The tilted v-flame is shown along the portion selected at the plane of the slit is marked. The size of the slit is exaggerated for a clear visual.

The measurements are taken by the same approach as earlier. 5 shots with an exposure time of 10 seconds each are taken followed by 5 background shots with the slit covered.

7.3.3. Results

Unlike the previous analysis the obtained signal is split into 3 sections which are analysed. The idea is that each of the section belongs to a separate portion of the flame front and variation along it can be captured. The sections selected consist of 11 binned pixels which is double the minimum of the pseudo-spatial resolution. The selected sections are shown in figure 7.11 with the direction of the reactive flow marked. The sections are numbered in increasing order from the reactants side towards the products side.

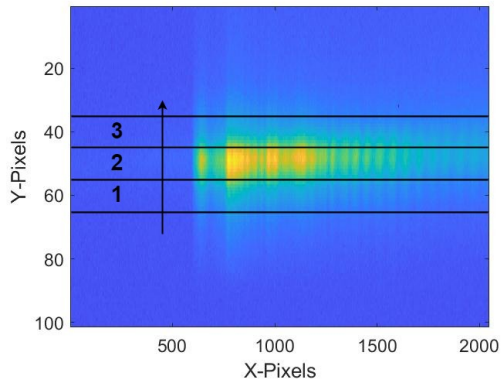

Figure 7.11: The ROI's selected for the sectional analysis are marked. The arrow marks the direction of the flow from the reactants side to the products side.

The temperature analysis is done similar to the previous study with the 2 case studies and the sub-cases with different wavelength ranges.

Case Study 1

The values of η and f_V are fairly constant. The temperature variation for the sub-cases A, B & C are presented in figure 7.12.

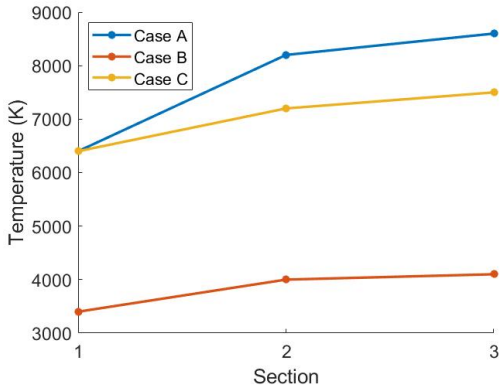

Figure 7.12: The variation of temperature across the different sections is shown for the sub-cases A,B and C.

The temperatures obtained is similar to the earlier case where the temperatures for sub-case B is much lower as compared to temperatures from the sub-cases A and C. In all the cases an increasing trend is observed with the section going from the reactants side to the products side. The difference in temperatures among the sections is highest for sub-case A. This is due to the large error introduced by the mismatch of the R_1 and R_2 peaks of the (0-0) band. The sub-cases B and C have a significant difference in temperature around 900 K between the sections but it is comparatively lower. The temperature values are tabulated in appendix A.

Case Study 2

As in the previous study, the rotational and vibrational temperatures are allowed to vary to check for a thermal

equilibrium. The temperatures are obtained for case study 2 with the sub-case D wavelength range. The vibrational and rotational temperatures obtained are shown in figure 7.13.

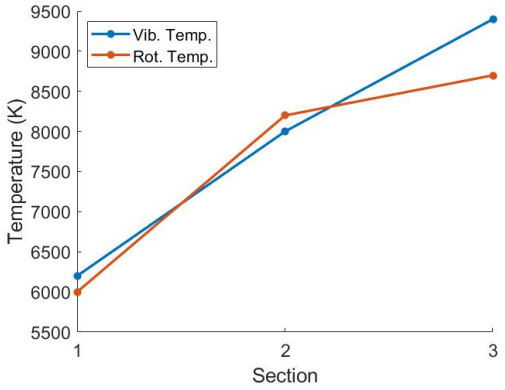

Figure 7.13: The variation of the rotational and vibrational temperature for the different sections is plotted. The wavelength range for the analysis is as per sub-case D.

In the figure 7.13, it is observed that the vibrational and rotational temperatures are relatively similar for the first 2 sections but differs strongly for section 3. The range of temperatures obtained is however very large varying by 3400 K. The temperature values are tabulated in appendix A.

7.3.4. Discussion

It should be mentioned upfront that the results of this study would not directly correspond to readings across the front. As mentioned in the experimental setup chapter, the spectrometer does not have confocal imaging capability. This implies that there is light coming from different sections of the flame apart from the plane in focus. The assumption in conducting this study was that the plane in focusing provides a strong signal but the light from other locations of the flame is uniformly distributed.

From theoretical calculations through CHEM1D, the adiabatic temperature variation across the flame front is known. The calculation is made for CH_4/air combustion at stoichiometric condition. If thermal equilibrium exists then the temperature from the region of the flame front where OH^* radicals exist can be obtained. The variation of the adiabatic temperature and the concentration of the OH radical are presented in figure 7.14.

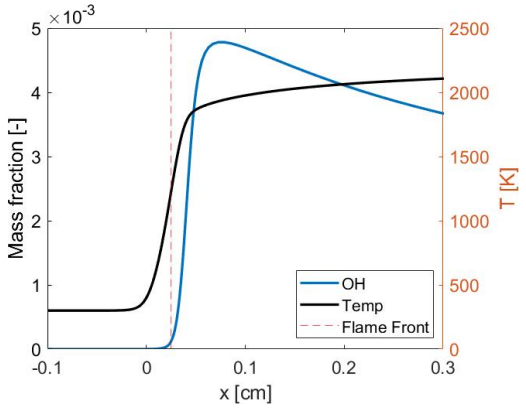

Figure 7.14: The figure contains the variation of the adiabatic flame temperature and the mass fraction variation of the OH radical across the flame front. The location of the flame front is marked by a red dashed line. The calculation is made for CH_4/air combustion at stoichiometric conditions.

The OH^* radical is present in a very localised region of the flame. The OH^* radical is located largely in the

region where the concentration of the OH radical is rising in concentration which roughly corresponds to a region about 0.4 mm in thickness. The variation of temperature if thermal equilibrium exists should be very small. In the result obtained the temperatures and the temperature variation obtained are much higher. The differences between the cases A,B and C are also similar to the first study. The temperatures obtained from the (0-0) vibrational band give comparatively lower temperatures from 3600 K to 4100 K.The values obtained with the temperature values from the stoichiometric case for the previous study can be compared. It is expected that the values should be close to the values of section 2 as this is the most intense part of the signal. This is however not seen in the temperatures obtained. The temperature from sub-case B is same for section 3 but the temperatures of sub-case A and C match the values of section 1 and then progressively increase to much higher values.

A surprising result appears for case study 2 with sub-case D wavelength range. As per the temperature values seen it appears as if thermal equilibrium exists as the vibrational and rotational temperatures match. However the temperature values obtained for the three sections are much higher than expected with values ranging from 6000 K to 9400 K. The rotational temperatures obtained in these sections is higher than the value of 5600 K from the previous study.

As mentioned earlier the results of this section is based on the assumption that light from other regions of the flame do not influence the quality of the spectrum from the plane in focus. However it is observed that the temperature values obtained do not align with the expected behaviour from theoretical calculations. The temperatures obtained are much higher than the adiabatic temperature similar to the earlier study. Also a variation in the spectra is observed across the sections which correspond to increasing temperature fits from the reactants side to the products side.

7.4. Disparity hypothesis

In all the temperature measurements, irrespective of equivalence ratio or whether it is rotational or vibrational temperature, the temperatures obtained are much higher than the adiabatic flame temperature. Also the temperatures given by the given (0-0) vibrational band is lower than the higher vibrational band. This implies a bias towards higher population in the higher state. There exists a disparity between the temperature observed through spectrum as compared to expected temperatures close to the adiabatic flame temperature. A hypothesis has been presented by Gaydon that the alternate chemical formation pathway in hydrocarbons is the cause of the disparity [7], [12].

$$CH + O_2 \rightleftharpoons OH^* + CO \quad \ldots 6.9\ eV$$

The mentioned pathway is highly exothermic and leads to the formation of OH^* with excess population in higher rotational and vibrational states. The collisional deactivation does bring the temperature lower but still is insufficient to bring it to a thermal equilibrium to give the gas temperature [7], [12].

7.5. Insight from other thermometry studies

The feasibility of gas temperature determination in flames from emission spectra of OH^* has not been achieved in the current flame. However studies with absorption spectra from OH provide temperatures close to the expected gas temperature [35], [36]. This implies that the ground state molecules are at thermal equilibrium as compared to the excited molecules. Even a recent study working with LIF on OH has found that the excited state has a non-thermalised population distribution with the higher vibrational state with excess population [37].

Apart from studies with a laminar premixed CH_4-air flames, this thermometry technique has also been applied on other flames with great success. A study conducted uses the intensity ratio of the vibrational branches with $\Delta v = 0$ and $\Delta v = 1$ to estimate the temperature in a turbulent CH_4-air flame [6]. In this study the temperatures obtained were close to the expected gas temperatures. This shows that even the Reynolds number has a key role to play in the collisional deactivation of the excited molecules.

8

Conclusions and Recommendations

This chapter brings the project to close by summarising the research project and the major outcomes of the project. It also highlights the various limitations of the methods followed in the project. A few recommendations based on insights gained during the project will also be mentioned along with ideas in which the current research can be taken forward.

8.1. Conclusions

The objective of the project was to model the emission spectrum of the OH^* radical and apply this model to compare with experimental measurements. One application for this comparison was suggested which is to measure the gas temperature in flames. The advantages of using a non-invasive, passive optical technique by capturing the chemiluminescence to measure temperature is that the gas flow in the flame is not disturbed.It does not require any additional equipment apart from a spectrometer to make the measurement making it a compact and easy to deploy tool.

The underlying physics for the spectroscopy in diatomic molecules are discussed in detail and then a model is developed for the emission spectra of the OH^* radical. The spectroscopic constants necessary to build the model are taken from literature and a model is implemented in MATLAB. In the current model the transition probabilities were calculated with simple models and correction factors were added to account for the interaction between the vibrational and rotational levels. This model is then compared to an industry standard spectroscopy tool LIFBASE to check the standard of the code.

After the completion of the model, an experimental setup was constructed to capture the emission spectra of the OH^* radical in the wavelength region of 300 nm to 330 nm. The grating angular calibration was done using a mercury lamp. The flame observed was a laminar v-flame generated by premixed CH_4-air combustion over a Bunsen burner. A finely resolved spectra with an instrument function of around 0.5 nm can be captured with the current spectrometer design which uses a reflective grating with 1200 lines per mm resolution. The camera used in the setup is an Andor Zyla 4.2 plus sCMOS camera which operates with a quantum efficiency of 5.5% to 12.5% in the wavelength range observed. The pseudo spatial resolution of the system with a v-flame was also determined with a razor blade across the slit. The pseudo spatial resolution of this system was obtained to be around 280 μm.

As one of the objective was to use the developed model to predict the gas temperature in a flame, the spectra from flames with equivalence ratios ranging from 0.8 to 1.2 were measured. The variation of adiabatic temperature across equivalence ratios is known from theoretical calculations using the CHEM1D application. Another variation of temperature within a flame is the variation of temperature across the flame front. This cannot be fully utilised as the emission from the OH^* radical emanates from a localised region of the flame front and temperature variation is very little. The spectra from flames of different equivalence ratios are fitted to the model using a least square error fit. The population distribution in the states is assumed to follow the Boltzmann distribution. The temperature fits are done across different wavelength ranges to compare spectra from the (0-0) vibrational band or both the (0-0) and (1-1) vibrational bands. Also, the vibrational and rotational temperatures are also allowed to vary independently to check for non-equilibrium behaviour.

The temperatures obtained when the experimentally obtained spectra are fit to the model are very high. The temperatures obtained vary from 4000 K to 7000 K rising with the equivalence ratio. The theoretical high-

est adiabatic temperature calculated from theory is around 2200 K at ϕ = 1.05. The estimated temperatures are much higher than equilibrium gas temperatures in flames. When only the (0-0) vibrational band region is fit the temperatures vary from 3200 K to 4100 K which are much lower as compared to when both vibrational bands exist in the fit which give temperatures from 4700 K to 6500 K. This suggests that there is a disparity in the population distribution and that the assumption of thermal equilibrium and Boltzmann distribution are not valid. This is further validated from the temperature values obtained when the vibrational and rotational temperatures are allowed to vary independently. The vibrational temperatures vary from 4800 K to 7500 K, whereas the rotational temperatures vary from 4400 K to 5800 K. The obtained rotational temperatures are consistent with measurements from literature in this particular case for laminar premixed CH_4-air combustion. This higher values of temperature is explained in literature by the production of OH^* through a chemical pathway involving the CH radical which produces the OH^* with excess population in the higher energy states. Even with collisional quenching, thermal equilibrium is not achieved in its emission lifetime. Even though the temperatures obtained do not correspond to the gas temperatures in the flame, these temperature are uniquely mapped to the equivalence ratio in the flames. This could be a potential application in flames where such an anomalous behaviour is observed.

Upon further investigation into literature, this excess population in higher states problem is seen only in hydrocarbon flames in laminar flames with low Reynolds number. A study with turbulent flames for CH_4-air combustion proves the feasibility of vibrational resolved OH^* spectra to determine temperature. Even though in the current experiment the feasibility of thermometry is not achieved there are various other regions where thermometry can be done. Apart from this application the model developed to simulate the OH^* spectrum can be used in various other applications as the model can be tuned to output the spectra for various instrument functions, line shapes and temperatures.

8.2. Recommendations

With the understanding gained during the process of this research project a few recommendations are suggested based on the limitations of the current work and possible future directions to take the current work forward.

- As simple formulas with broad assumptions were used for transition probability calculations, the OH^* emission model can be improved by implementing better methods for line strength calculations.
- The OH^* emission model can also be improved such that population distributions can be fit directly for a given spectra instead of assuming Boltzmann distribution. This would help in fitting non-equilibrium spectra.
- Conduct experiments with a turbulent flame to test the results from the other study which show thermal behaviour in this flow regime.
- Conduct experiments with a H_2-Air flame to test the theory predicting OH^* production with excess population in higher states for hydrocarbon fuels to ascertain the hypothesis.
- If experimental spectra can be obtained for high pressure or high temperature flames such as rocket flames, test the feasibility of thermometry through OH^* spectra in such flames. In such flames the intensity is also quite high allowing for low exposure times which would help in capturing dynamics of the flame also is necessary.

A

Temperature values from the spectrum fits

A.1. Variation with equivalence ratio

A.1.1. Case study 1

ϕ	**sub-case A** (K)	**sub-case B** (K)	**sub-case C** (K)
0.8	4300	3200	4700
0.9	5100	3700	5500
1.0	6400	4100	6000
1.1	6600	4100	6100
1.0	6900	4100	6500

A.1.2. Case study 2

ϕ	$\mathbf{T_{vib}}$ (K)	$\mathbf{T_{rot}}$ (K)
0.8	4800	4400
0.9	6100	5000
1.0	6900	5600
1.1	7200	5700
1.0	7500	5800

A.2. Variation across the flame front

A.2.1. Case study 1

Section	**sub-case A** (K)	**sub-case B** (K)	**sub-case C** (K)
1	6400	3400	6400
2	8200	4000	7200
3	8600	4100	7500

A.2.2. Case study 2

Section	$\mathbf{T_{vib}}$ (K)	$\mathbf{T_{rot}}$ (K)
1	6200	6000
2	8000	8200
3	9400	8700

Bibliography

[1] A. G. Rao, F. Yin, and J. P. van Buijtenen, "A hybrid engine concept for multi-fuel blended wing body", *Aircraft Engineering and Aerospace Technology: An International Journal*, 2014.

[2] "Destination green: The next chapter", International Civil Aviation Organisation, Environmental Report, 2019, ch. Chapter 1 – Aviation and the Environment: Outlook. [Online]. Available: https://www.icao.int/environmental-protection/Pages/envrep2019.aspx.

[3] J. Warnatz, U. Maas, R. W. Dibble, and J. Warnatz, *Combustion: Physical and Chemical Fundamentals, Modeling and Simulation, Experiments, Pollutant Formation*, 3rd ed. Springer, 2001.

[4] Chem1D, *One-dimensional laminar flame code, eindhoven university of technology*, 2012.

[5] A. A. Perpignan, A. Gangoli Rao, and D. J. Roekaerts, "Flameless combustion and its potential towards gas turbines", *Progress in Energy and Combustion Science*, vol. 69, pp. 28–62, 2018, ISSN: 0360-1285. DOI: https://doi.org/10.1016/j.pecs.2018.06.002.

[6] M. Lauer and T. Sattelmayer, "Determination of turbulent flame temperature from vibrationally resolved oh* chemiluminescence measurements", Jan. 2009.

[7] A. G. Gaydon, *The Spectroscopy of Flames*, 2nd ed. London: Chapman and Hall, 1974.

[8] J. M. Hall and E. L. Petersen, "An optimized kinetics model for oh chemiluminescence at high temperatures and atmospheric pressures", *International journal of chemical kinetics*, vol. 38, no. 12, pp. 714–724, 2006.

[9] E. K. Plyler and C. Humphreys, "Flame spectrum of acetylene from 1 to 5 microns", *Journal of Research of The National Bureau of Standards*, vol. 42, no. 6, pp. 567–572, 1949.

[10] J. Kojima, Y. Ikeda, and T. Nakajima, "Basic aspects of oh (a), ch (a), and c2 (d) chemiluminescence in the reaction zone of laminar methane–air premixed flames", *Combustion and Flame*, vol. 140, no. 1-2, pp. 34–45, 2005.

[11] G. Zizak, "Flame emission spectroscopy: Fundamentals and applications", 2000.

[12] R. Mavrodineanu and H. Boiteux, "Flame spectroscopy", in, ser. Allen series : Wiley series in pure and applied spectroscopy. J. Wiley, 1965, pp. 329–361, ISBN: 978-04-715-7830-7.

[13] R. N. Dixon, "The carbon monoxide flame bands", *Proceedings of the Royal Society of London. Series A. Mathematical and Physical Sciences*, vol. 275, no. 1362, pp. 431–446, 1963.

[14] J. M. Samaniego, F. N. Egolfopoulos, and C. T. Bowman, "Co2* chemiluminescence in premixed flames", *Combustion Science and Technology*, vol. 109, no. 1-6, pp. 183–203, 1995.

[15] G. Fowles, *Introduction to Modern Optics*, ser. Dover Books on Physics Series. Dover Publications, 1989, ISBN: 9780486659572.

[16] C. A. Palmer and E. G. Loewen, *Diffraction grating handbook*. Thermo RGL New York, 2002, vol. 5.

[17] W. S. Boyle and G. E. Smith, "Charge coupled semiconductor devices", *Bell System Technical Journal*, vol. 49, no. 4, pp. 587–593, 1970.

[18] Andor, *Ccd architectures*, Accessed on : 23-12-2020. [Online]. Available: https://andor.oxinst.com/learning/view/article/ccd-sensor-architectures.

[19] E. R. Fossum, "Active pixel sensors: Are ccds dinosaurs?", in *Charge-Coupled Devices and Solid State Optical Sensors III*, International Society for Optics and Photonics, vol. 1900, 1993, pp. 2–14.

[20] D. George, *Ccd versus cmos: Which is better?*, Accessed on : 23-12-2020. [Online]. Available: https://diffractionlimited.com/ccd-versus-cmos-better/.

[21] S. Meroli, *Active pixel sensor vs ccd. who is the clear winner?*, Accessed on : 23-12-2020. [Online]. Available: https://meroli.web.cern.ch/lecture_cmos_vs_ccd_pixel_sensor.html.

[22] G. Herzberg, *The Spectra and Structures of Simple Free Radicals : An Introduction to Molecular Spectroscopy*. Cornell University Press, 1971.

[23] ——, *Molecular Spectra and Molecular Structure I : Spectra of Diatomic Molecules*, 2nd ed. D. Van Nostrand Company, Inc., 1950.

[24] G. Dieke and H. Crosswhite, "The ultraviolet bands of oh fundamental data", *Journal of Quantitative Spectroscopy and Radiative Transfer*, vol. 2, no. 2, pp. 97–199, 1962.

[25] A. Schadee, "Unique definitions for the band strength and the electronic-vibrational dipole moment of diatomic molecular radiative transitions", *Journal of Quantitative Spectroscopy and Radiative Transfer*, vol. 19, no. 4, pp. 451–453, 1978, ISSN: 0022-4073. DOI: https://doi.org/10.1016/0022-4073(78)90120-6.

[26] L. T. Earls, "Intensities in Π 2- Σ 2 transitions in diatomic molecules", *Physical Review*, vol. 48, no. 5, p. 423, 1935.

[27] J. Anketell and R. Learner, "Vibration rotation interaction in oh and the transition moment", *Proceedings of the Royal Society of London. Series A. Mathematical and Physical Sciences*, vol. 301, no. 1466, pp. 355–361, 1967.

[28] G. K. Wertheim, M. A. Butler, K. W. West, and D. N. E. Buchanan, "Determination of the gaussian and lorentzian content of experimental line shapes", *Review of Scientific Instruments*, vol. 45, no. 11, pp. 1369–1371, 1974. DOI: 10.1063/1.1686503.

[29] T. Ida, M. Ando, and H. Toraya, "Extended pseudo-Voigt function for approximating the Voigt profile", *Journal of Applied Crystallography*, vol. 33, no. 6, pp. 1311–1316, Dec. 2000. DOI: 10.1107/S0021889800010219.

[30] J. Olivero and R. Longbothum, "Empirical fits to the voigt line width: A brief review", *Journal of Quantitative Spectroscopy and Radiative Transfer*, vol. 17, no. 2, pp. 233–236, 1977, ISSN: 0022-4073. DOI: https://doi.org/10.1016/0022-4073(77)90161-3.

[31] J. Luque and D. R. Crosley, "Lifbase: Database and spectral simulation program (version 1.9)", *SRI international report MP*, vol. 99, no. 009, 1999.

[32] Thorlabs, *400 nm blaze wavelength reflective diffraction gratings*, Accessed on : 02-01-2021. [Online]. Available: https://www.thorlabs.com/newgrouppage9.cfm?objectgroup_id=8626.

[33] Andor, *Quantum efficiency - andor zyla 4.2 plus*, Personal Communication, William Fresquet.

[34] J. Zhao, "Image curvature correction and cosmic removal for high-throughput dispersive raman spectroscopy", *Applied spectroscopy*, vol. 57, no. 11, pp. 1368–1375, 2003.

[35] H. P. Broida, "Rotational temperatures of oh in methane-air flames", *The Journal of Chemical Physics*, vol. 19, no. 11, pp. 1383–1390, 1951.

[36] A. G. Gaydon, G. Spokes, and J. V. Suchtelen, "Absorption spectra of low-pressure flames", *Proceedings of the Royal Society of London. Series A. Mathematical and Physical Sciences*, vol. 256, no. 1286, pp. 323–333, 1960.

[37] A. Jain, Y. Wang, and W. D. Kulatilaka, "Simultaneous imaging of h and oh in flames using a single broadband femtosecond laser source", *Proceedings of the Combustion Institute*, 2020, ISSN: 1540-7489. DOI: https://doi.org/10.1016/j.proci.2020.07.137.